

AD-778 458

NEAR-FIELD OBSERVATIONS AND SOURCE
PARAMETERS OF CENTRAL CALIFORNIA
EARTHQUAKES

Lane R. Johnson, et al

California University

Prepared for:

Air Force Office of Scientific Research

December 1973

DISTRIBUTED BY:

NTIS

National Technical Information Service
U. S. DEPARTMENT OF COMMERCE
5285 Port Royal Road, Springfield Va. 22151

UNCLASSIFIED

Security Classification

DOCUMENT CONTROL DATA - R & D

(Security classification of title, body of abstract and indexing annotation must be entered when the overall report is classified)

1. ORIGINATING ACTIVITY (Corporate author)

University of California, Berkeley
Geology and Geophysics
Berkeley, CA 94720

20. REPORT SECURITY CLASSIFICATION

UNCLASSIFIED

21. GROUP

3. REPORT TITLE

NEAR-FIELD OBSERVATIONS AND SOURCE PARAMETERS OF CENTRAL CALIFORNIA EARTHQUAKES

4. DESCRIPTIVE NOTES (Type of report and inclusive dates)

Scientific....

5. AUTHOR(S) (First name, middle initial, last name)

Lane R. Johnson and Thomas V. McEvilly

6. REPORT DATE

December, 1973

7a. TOTAL NO. OF PAGES

66

7b. NO. OF REFS

22

8a. CONTRACT OR GRANT NO.

AFOSR-72-2392

b. PROJECT NO.

AO 1827-7

c.

62701E

d.

9a. ORIGINATOR'S REPORT NUMBER(S)

9b. OTHER REPORT NO(S) (Any other numbers that may be assigned)

AFOSR - TR - 74 - 0635

10. DISTRIBUTION STATEMENT

Approved for public release; distribution unlimited.

Reproduced by
NATIONAL TECHNICAL
INFORMATION SERVICE
U. S. Department of Commerce
Springfield, VA 22151

11. SUPPLEMENTARY NOTES

TECH, OTHER

12. SPONSORING MILITARY ACTIVITY

AR Office of Scientific Research/NP
1400 Wilson Boulevard Arlington, VA
Arlington, VA 22209

13. ABSTRACT

This is a study of source characteristics of 13 earthquakes with magnitudes between 2.4 and 5.1 located near the San Andreas fault in central California. On the basis of hypocentral locations and fault plane solutions the earthquakes separate into two source groups, one group clearly related to the throughgoing northwest trending San Andreas fault zone and the other apparently associated with generally north trending bifurcations such as the Calaveras fault. The basic data consist of broadband recordings (0.03 to 10 Hz) of these earthquakes at two sites of the San Andreas Geophysical Observatory (SAGO). Epicentral distances range between 2 and 40 km, and maximum ground displacements from 4 to 4000 microns were recorded. The whole-record spectra computed from the seismograms lend themselves to source parameter studies in that they can be interpreted in terms of low-frequency level, corner frequency, and high-frequency slope. The influence of tilts and nonlinear response of the seismometer was considered in the interpretation of the low frequencies. Seismic source moments estimated from the low-frequency levels of the spectra show a linear dependence upon magnitude with a slope slightly greater than 1. The geology at the recording site can contribute an uncertainty factor of at least 3 to the estimated moments. Synthetic seismograms have also been used to estimate seismic moments in both the time domain and frequency domain, and the results compare favorably with those estimated directly from the low-frequency levels of the spectra. Observed corner frequencies are only weakly dependent upon magnitude. Interpreted in terms of source dimension, these corner frequencies imply values of 1 to 2 km for the earthquakes of this study. The corner frequencies may also be interpreted

DD FORM 1473

(abstract continued on reverse)

UNCLASSIFIED

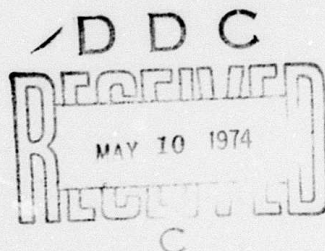
14. KEY WORDS	LINK A		LINK B		LINK C	
	ROLE	WT	ROLE	WT	ROLE	WT
earthquakes source parameters central California San Andreas fault seismic spectra seismic moments earthquake source models near field						
(abstract continued) in terms of the rise time of the source function, yielding values in the range 0.5 to 1.0 sec. The data indicate that the earthquakes of this study are all surprisingly similar in their source parameters, with only the seismic moment showing a strong dependence on magnitude.						

AD778458

NEAR-FIELD OBSERVATIONS AND
SOURCE PARAMETERS OF CENTRAL CALIFORNIA EARTHQUAKES

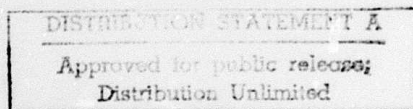
Lane R. Johnson and Thomas V. McEvilly

Seismographic Station
Department of Geology and Geophysics
University of California
Berkeley, California 94720



AIR FORCE OFFICE OF SCIENTIFIC RESEARCH (AFSC)
NOTICE OF TRANSMITTAL TO DDC
This technical report has been reviewed and is
approved for public release IAW AFR 190-12 (7b).
Distribution is unlimited.

D. W. TAYLOR
Technical Information Officer



Reproduced by
NATIONAL TECHNICAL
INFORMATION SERVICE
U S Department of Commerce
Springfield VA 22151

ABSTRACT

This is a study of source characteristics of 13 earthquakes with magnitudes between 2.4 and 5.1 located near the San Andreas fault in central California. On the basis of hypocentral locations and fault plane solutions the earthquakes separate into two source groups, one group clearly related to the throughgoing northwest trending San Andreas fault zone and the other apparently associated with generally north trending bifurcations such as the Calaveras fault. The basic data consist of broadband recordings (0.03 to 10 Hz) of these earthquakes at two sites of the San Andreas Geophysical Observatory (SAGO). Epicentral distances range between 2 and 40 km, and maximum ground displacements from 4 to 4000 microns were recorded. The whole-record spectra computed from the seismograms lend themselves to source parameter studies in that they can be interpreted in terms of low-frequency level, corner frequency, and high-frequency slope. The influence of tilts and nonlinear response of the seismometer was considered in the interpretation of the low frequencies. Seismic source moments estimated from the low-frequency levels of the spectra show a linear dependence upon magnitude with a slope slightly greater than 1. The geology at the recording site can contribute an uncertainty factor of at least 3 to the estimated moments. Synthetic seismograms have also been used to estimate seismic moments in both the time domain and frequency domain, and the results compare favorably with those estimated directly from the low-frequency levels of the spectra. Observed corner frequencies are only weakly dependent upon magnitude. Interpreted in terms of source dimension, these corner frequencies imply values of 1 to 2 km for the earthquakes of this study. The corner frequencies may also be interpreted in terms of the rise time of the source function, yielding values in the range 0.5 to 1.0 sec. The data indicate that the earthquakes of this study are all surprisingly similar in their source parameters, with only the seismic moment showing a strong dependence on magnitude.

INTRODUCTION

In 1966-67 the San Andreas Geophysical Observatory (SAGO) was established on the San Andreas fault zone in central California some 5 miles south of Hollister. The primary purpose of the observatory is the long-term study of various geophysical phenomena associated with an active segment of the fault zone. A variety of seismometers recording on magnetic tape monitor local earthquakes in the magnitude range from microearthquakes of $M_L = -1$ and less up through strong local shocks of $M_L = 5$ or more with displacements of several mm. The seismometers plus tilt and strain meters, magnetometers, telluric current monitors, and others are distributed along the fault zone in a region about 5 km square.

SAGO is located between two clusters of earthquake activity which form the main concentrations of ongoing moderate seismicity in central California. Within 50 km along the San Andreas fault zone to the southeast of SAGO lies the seismically active Stone Canyon and Bear Valley region, while the same distance to the northwest includes the clusters of seismicity near San Juan Bautista and Corralitos. In this 100 km length along the San Andreas fault zone, centered at SAGO and including the bifurcation with the Calaveras fault, occur most central California earthquakes (Bolt et al., 1968; Bolt and Miller, 1971), with an average over recent years of about one event per year with M_L greater than 4.5. Earthquake mechanisms are generally of right-lateral, transcurrent type. Fault slippage through creep is observed on both the San Andreas and Calaveras fault traces in the region, with average slip rates exceeding 1 cm/yr at some localities. This area is undoubtedly one of the most heavily instrumented and thoroughly studied regions of earthquake activity in the world.

This study is an investigation of near-field radiation from local earthquakes recorded on broadband seismometer systems at SAGO. From the library of events preserved on magnetic tape, 13 earthquakes were selected with a magnitude range of 2.4 to 5.1, an epicentral distance range of 2 to 40 km, and a variety of apparent source geometries relative to the main throughgoing San Andreas fault trace. The data set samples a range of magnitudes at a given distance for one type of comparison and a range of distances at a given magnitude for another.

Motivation for near-field studies comes from several areas. By making observations with broadband instrumentation within a few source depths, source dimensions, or wavelengths one would hope to obtain better definition of the detailed structure in the radiated waves and consequently improve the ability to make inferences on a specific earthquake source model. In addition to the scientific gain in increased knowledge of the source, differentiation among alternative models with subtle variations in radiated waves is important in understanding the basis for observed discriminants between earthquakes and explosions. Finally, specification of a working model for the dynamics of an earthquake source can lead to direct computation of strong motion in the near-field of potentially damaging earthquakes, and thus provide additional capability in determining design earthquake motions in earthquake engineering practice.

DATA

Figure 1 shows the 2 SAGO seismographic stations and 13 earthquakes involved in this study. The SAGO-Central station (SAO) is 2 km southwest of the San Andreas fault trace in the granitic rocks of the Cabilan range. SAGO-East, the other station with broadband instruments suitable for this study, lies 4 km northeast of the fault trace in a band of exposed Pliocene sedimentary rocks between the fault and the extensive Franciscan outcrop farther to the northeast. The coordinates of the stations are:

SAGO-Central	36° 45.90' N	121° 26.80' W
SAGO-East	36° 48.44' N	121° 24.44' W

Seismic wave velocities differ across the San Andreas fault zone in this region. Near-surface P velocities are about 5.3 and 4.8 km/sec southwest and northeast, respectively of the fault zone and increase fairly uniformly to a common value of about 6.0 km/sec at a depth of 10 km, below which the rate of velocity increase with depth is appreciably smaller (Chuaqui and McEvilly, 1968).

Table 1 is a summary of data on the 13 earthquakes studied and lists hypocentral and focal mechanism parameters in addition to distances and azimuths to the two SAGO stations. Hypocentral locations for these earthquakes are considered to be of excellent quality with complete azimuthal station coverage and well-determined station corrections available. However, the effects of velocity differences across the fault are difficult to completely remove, and systematic errors still remain in the locations. Experience with both earthquake and explosion sources in this region suggests that earthquakes in regions 1, 2, and 5 (Figure 1) are off the San Andreas fault, while events in regions 3, 4, and 6 represent slip on the main San Andreas fault. The relation of events in region 7 to the San Andreas fault remains unclear.

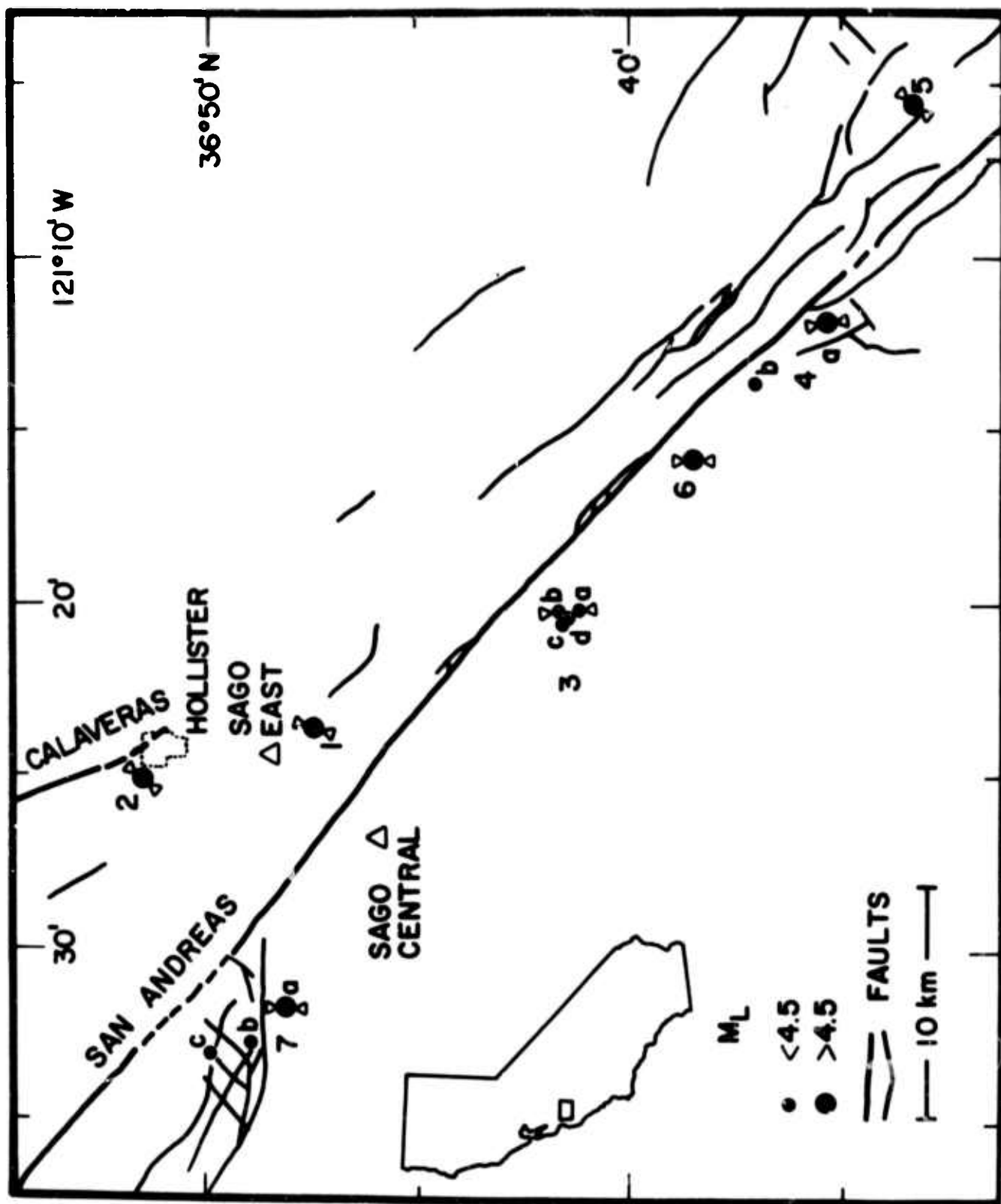


Figure 1. A map of part of central California showing the primary mapped fault traces, the location of the seismographic stations at SAGO-Central and SAGO-East, and the epicenters of the 13 earthquakes studied. The identification numbers key the earthquakes to Table 1. The open triangles associated with the larger earthquakes denote the directions of principal compression as determined from fault plane solutions (Figure 2).

Table 1. Data summary for earthquakes

Event Number	Location	Date	Origin Time h m s	M _L	Coordinates d m	Depth km	SAGO-C		SAGO-E		Strike Princ Fault Comp Plane
							Dist km	Az deg	Dist km	Az deg	
1	Harris Ranch	27 Oct 69	10 59 42.8	4.6	36 17.4 N 121 23.6 W	12.5	5.5	240	2.3	274	N13E N32W
2	Hollister	13 Mar 70	07 02 28.6	4.7	36 51.5 N 121 25.1 W	10.2	10.6	194	5.7	170	N39E N06W
3a	Limekiln Road	29 Dec 71	00 25 35.7	4.0	36 41.2 N 121 20.1 W	3.7	13.2	311	14.8	334	N06W N49W
3b		01 06 30.7	2.6	36 41.7 N 121 20.2 W	4.6	12.5	308		14.0	333	
3c		01 37 13.7	3.7	36 41.6 N 121 20.6 W	4.0	12.2	311		13.9	336	
3d		01 55 47.7	2.4	36 41.4 N 121 20.4 W	3.6	12.6	311		14.3	335	
4a	Melendy Ranch	24 Feb 72	15 56 51.3	5.1	36 35.3 N 121 11.8 W	6.4	29.7	311	30.7	322	N09W N55W
4b		20 21 48.7	3.6	36 37.0 N 121 13.6 W	7.6	25.6	310		26.6	323	
5	San Benito	27 Feb 72	22 13 08.6	4.7	36 33.3 N 121 05.6 W	10.6	39.3	306	39.7	315	N39E N05W(?) N95W
6	Stone Canyon	04 Sep 72	18 04 40.9	4.7	36 38.5 N 121 15.8 W	5.1	21.3	310	22.4	325	N01E N45W
7a	San Juan Bautista	03 Oct 72	06 30 02.0	4.9	36 48.1 N 121 31.7 W	5.2	8.3	120	10.8	87	N01E N80W
7b		11 10 13.3	4.1	36 48.9 N 121 32.7 W	5.1	10.4	122		12.3	94	
7c		04 Oct 72	08 41 05.6	3.0	36 49.9 N 121 33.1 W	4.3	12.0	128	13.2	102	

Sources for these earthquakes can be modeled by right-lateral transcurrent faulting on planes roughly parallel to the San Andreas fault zone. Fault plane solutions for the largest event in each of the regions are presented in Figure 2. While a right-lateral slip interpretation is consistent with all the solutions, events 5 and 7a may well be left-lateral slip on the conjugate plane. A striking consistency is apparent in the orientation of the axes of compression as inferred from the first motion data. Arrows in Figures 1 and 2 show the horizontal projections of these compression axes. Earthquakes on or to the southwest of the San Andreas fault show axes oriented uniformly north-south, as expected, while in regions northeast of the fault the compression axes trend nearly normal to the San Andreas. This normal trend is consistent with the strike of the Calaveras fault zone to the north and thus is not unexpected at event 2, but it seems odd at event 5 where it may indicate a tendency to bifurcation. Another unique property of the 3 earthquakes with compression axes in the northeast-southwest direction is a focal depth greater than 10 km (Table 1).

Instruments providing the data for this investigation are conventional long-period pendulums of WSSN type which are equipped with displacement transducers and record on FM analog magnetic tape with a 0-10 Hz bandwidth. At SAGO-East natural periods are 15 sec and only horizontal instruments are operated. At SAGO-Central a three-component system operates with natural periods of 30 sec, and velocity outputs are recorded in addition to displacements but at higher sensitivities. Signals are digitized from the analog FM tapes with full scale values equal to ± 2048 counts. The resulting sensitivities for the three types of data channels are given in Figure 3.

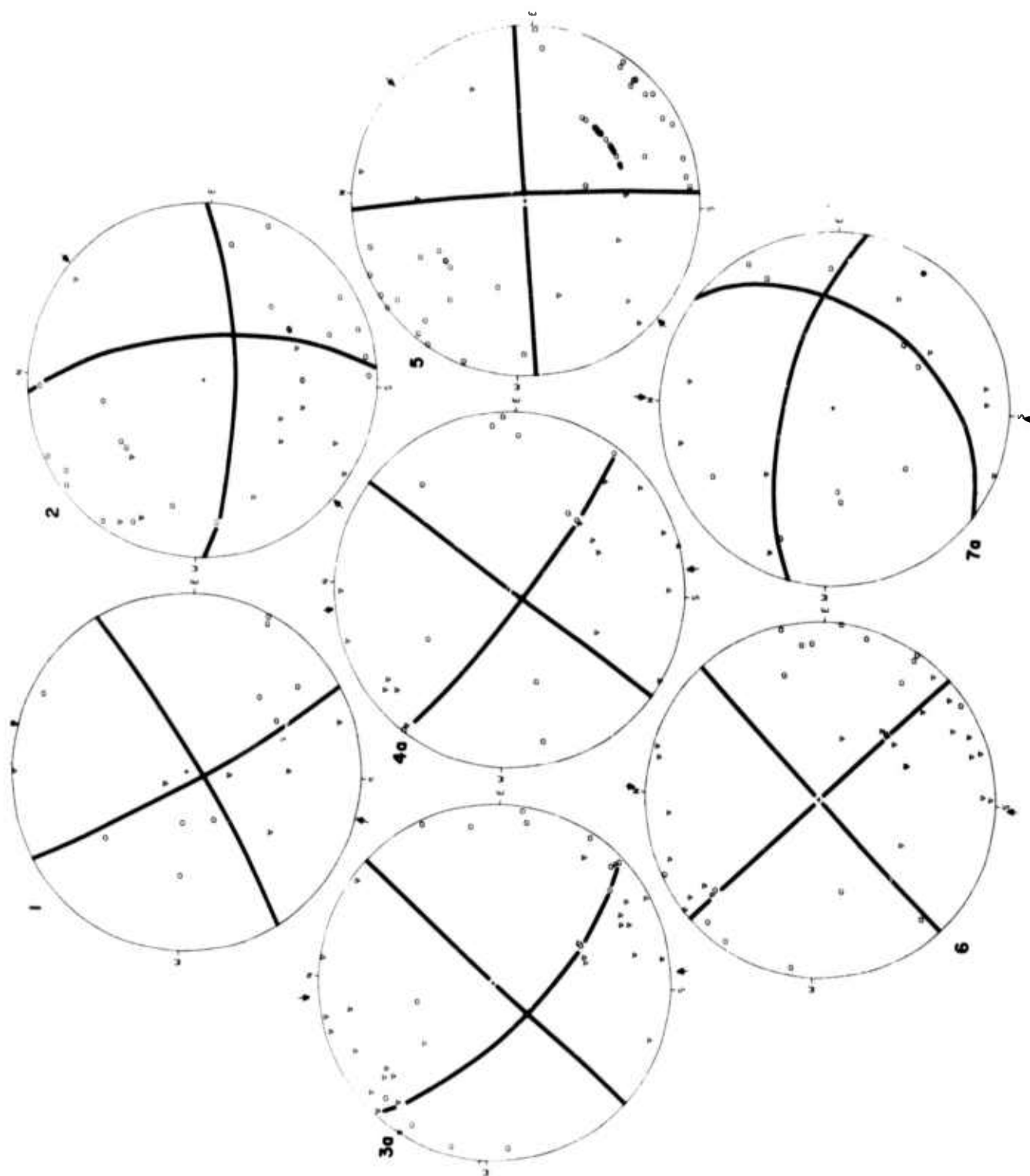


Figure 2. Upper hemisphere projections of the polarity of P waves from 7 of the larger earthquakes in Table 1 and the fault plane solutions determined on the basis of these data. Circles denote compressions and triangles denote dilatations. Arrows indicate the horizontal projections of the principal compressive stress. The identification numbers key the earthquakes to Table 1 and Figure 1.

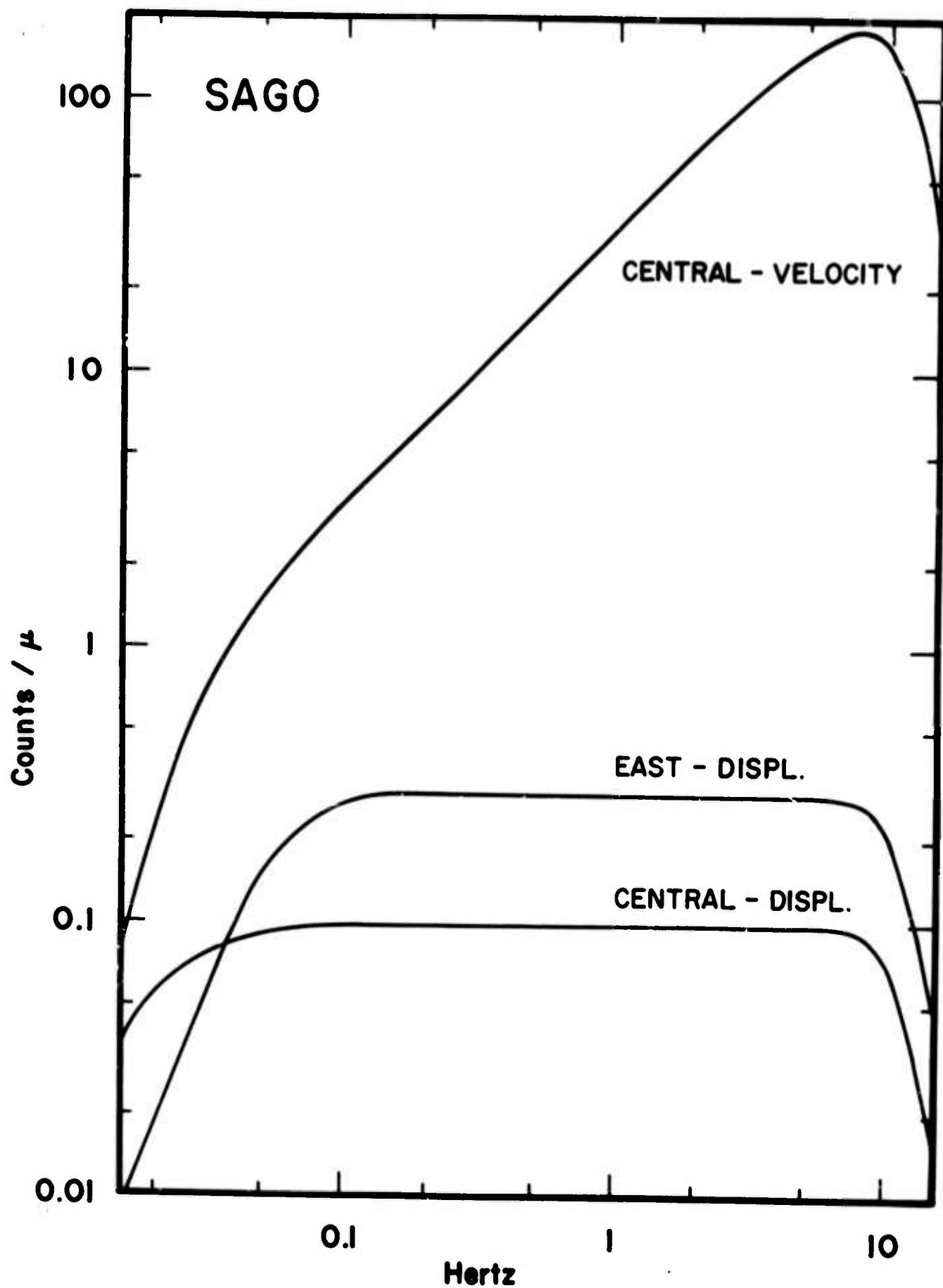


Figure 3. The displacement response functions of three types of seismographs at SAGO which were used in this study. The ordinate is in terms of output from a ± 2048 count A/D system.

ANALYSIS

The data considered in this study are rather unique in that they are broadband recordings (bandwidth from .03 to 10 Hz) of ground displacement near to earthquake sources (epicentral distances from 2 to 40 km). While there are advantages to working with data recorded so near the source, there are also problems not usually encountered in the analysis of far-field data. Thus it seems appropriate to describe some general aspects of the data and the analysis procedures which have been applied.

Figure 4 presents a complete data set for one earthquake. In the upper part are the time traces and spectra for the two horizontal components at SAGO-East. The time traces are not corrected for the instrument response. In view of the broad flat response characteristics shown in Figure 3 it is clear that these traces closely approximate ground displacement. Corrections for the seismometer and all other components in the data acquisition system have been applied to the spectra so they represent actual ground displacement. In the lower part of Figure 4 are the time traces of displacement and displacement spectra for the three-component set of instruments at SAGO-Central. As mentioned earlier, the instruments at SAGO-Central have velocity and displacement transducers at different gains. During the analysis the velocity output signals are integrated in the frequency domain with a 40 sec 1 pole high-pass filter simultaneously applied to eliminate base-line drift. The time traces for SAGO-Central in the figure are such displacement records obtained by integrating the velocity output signals.

The displacement traces in Figure 4 illustrate an important characteristic of near-field seismic data in that the various seismic waves are not isolated arrivals on the seismograms. The P wave is typically small but increases

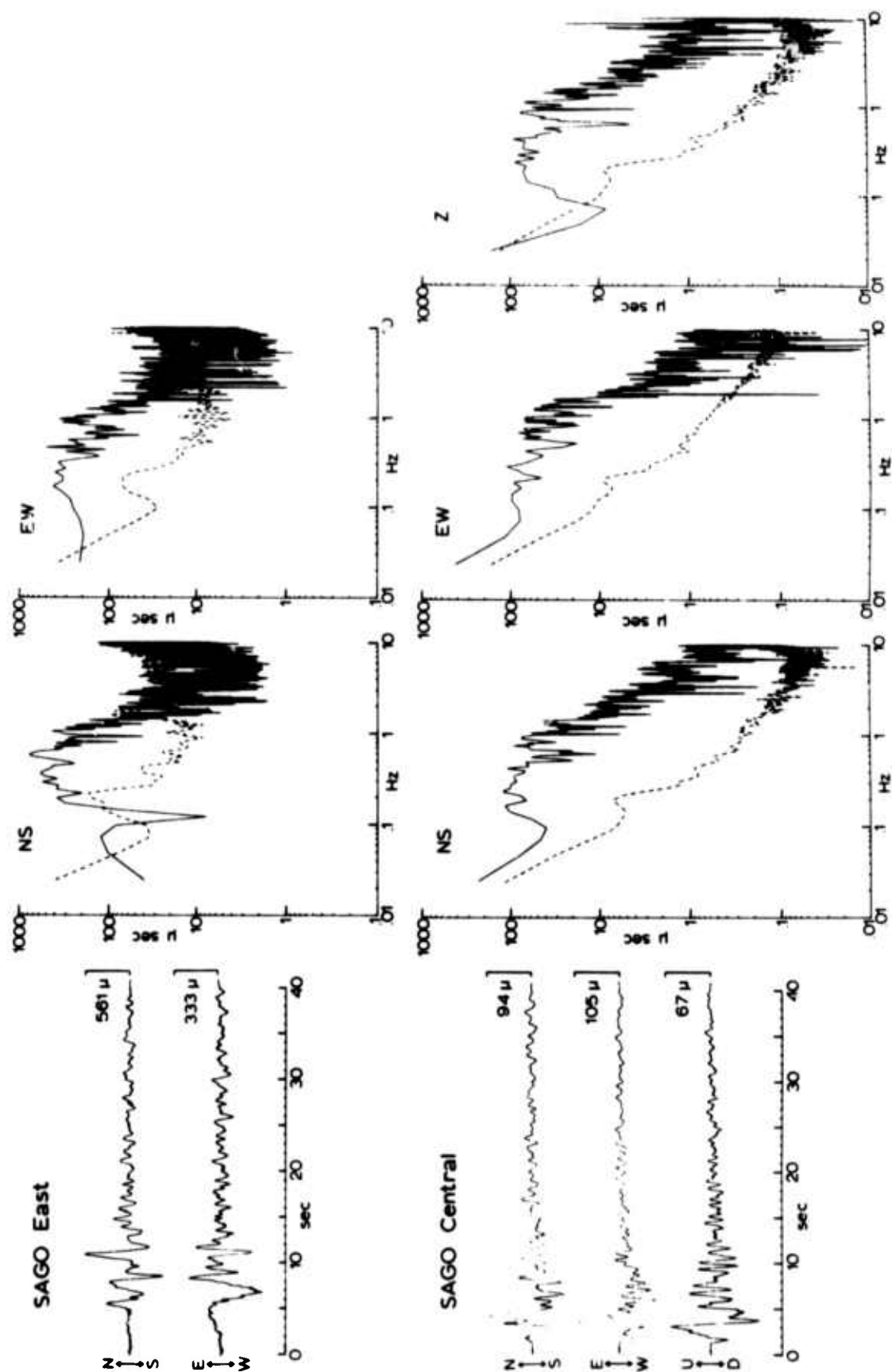


Figure 4. The displacement seismograms and spectra recorded at SAGO-East (top) and SAGO-Central (bottom) from event 7b (Table 1). The plots of spectra show the amplitude density spectra for both the signal (solid line) and an estimate of the noise (dashed line).

gradually until it merges with the much larger S wave which in turn is followed by a lengthy and sometimes large coda. Note that the SAGO-East station is near a P nodal line so that the P arrival (at about 2 sec in the figure) is particularly small. It is obvious that it would be difficult to identify, isolate, and compute a spectrum for either the P or S wave alone, and that the truncation effects introduced in such a process could be severe. For this reason the spectra in this study were all computed from the whole record with no attempt to isolate individual wave arrivals. The rationale behind this approach is that all arrivals on the seismogram, whatever their mode of propagation, are excited by the same source and thus should carry its spectral signature. Interference between the various arrivals can be expected to introduce considerable irregularity into the spectra (usually referred to as spectral scalloping), but numerical experiments with near-field synthetic seismograms have indicated that the salient features of the source spectrum are preserved in the whole-record spectra.

All spectra in this study were computed from a 41 sec time window which is the length of the time traces in Figure 4. This time window is long enough to allow the coda to decay to a reasonably small value, and truncation effects are further avoided by smoothly tapering the last 2 sec of the time window. Note that this time window is longer than the significant portions of the impulse response functions for the 15 and 30 sec pendulums employed in this study. The spectra are calculated with a discrete form of the Fourier transform defined in terms of the frequency f in Hz and thus do not involve a normalization factor of 2π (system 1 of Bracewell, 1965, p. 7).

The spectra in Figure 4 all contain a dashed line which is an estimate of the noise present at the time of the earthquake. These estimates were computed from the time trace during the minute preceding the earthquake. The analysis procedures for the noise and signal were identical except that a Hanning window was applied to the noise estimate. The solid line

in the plots is an estimate of the amplitude spectral density of the signal obtained by subtracting the noise estimate from the spectrum which was computed from the time trace during the earthquake. The estimate of the noise spectrum is helpful in assessing the significance of various features of the signal spectrum.

The data were sampled at a rate of 50 samples per sec to give a Nyquist frequency of 25 Hz. The analog signal was strongly filtered beyond 10 Hz to avoid aliasing and noise problems (see Figure 3). Spectral estimates at frequencies above 10 Hz consist of a small signal strength magnified by a large instrument correction factor (particularly in the case of the displacement channels) and are considered less reliable than those at lower frequencies. For this reason frequencies above 10 Hz are not considered in this study. At low frequencies the affect of the instrument correction is not so pronounced and all spectral estimates falling above the noise level are considered to be reliable. However, as will be discussed later, the conventional long-period instruments employed in this study are susceptible to tilts and spurious transients which affect the low frequencies, so considerable care must be taken in interpreting this part of the spectrum. The type of vertical seismometer at SAGO-Central is known to be susceptible to nonlinear parasitic vibrations during strong shaking, and thus data from this instrument have received much less emphasis than those of the horizontal components.

The spectra obtained in this study are amenable to the usual interpretation in terms of low-frequency level, corner frequency, and high-frequency slope. The spectra are typically fairly flat in the frequency range 0.1 to 1 Hz and the low-frequency level, Ω_0 , was estimated from this portion of the spectrum. At frequencies less than 0.1 Hz the spectra are much more variable (see, for example, Figure 4). Beyond about 2 Hz all of the spectra

show a pronounced decrease with increasing frequency which is fairly linear on a log-log plot and typically has a slope of about -2 to -3. In Figure 4 the spectra from the displacement transducers reverse their slope and begin to increase beyond about 5 Hz, but this is clearly due to the presence of noise.

Several different approaches to the problem of estimating the spectral characteristics of low-frequency level, corner frequency, and high-frequency slope were investigated, and the one finally used and described here seemed to be less subjective than the others. The frequency response of a Butterworth low-pass filter modified to include the effects of attenuation was selected as an analytical model for the spectra. Figure 5 shows this spectral model for high-frequency slopes of -2 and -3 and four values of attenuation. The effect of attenuation is taken to be $\exp(-\pi f t^*)$ where f is frequency and t^* is the travel time divided by the average quality factor Q . For the S waves in this study the travel time varies between about 3 and 10 sec, Q values between 30 and 300 are reasonable for these paths (O'Neill and Healy, 1973; Kurita, 1973), and f_0 is in the range of 1 to 3 Hz so a range in $f_0 t^*$ from 0.3 to 0.01 covers most of the possible cases. The low-frequency level, Ω_0 , and the corner frequency, f_0 , are identified in the figures. These figures are used as templates to be overlain on the observed spectra, shifted to obtain what the eye judges to be a best fit, and then used to read off values of Ω_0 and f_0 . The method is illustrated in Figure 6 with an observed spectrum and two analytical curves which are judged to fit it about equally well. Note that the analytical curves are fit to the observed spectrum as envelopes. Usually the ranges between 0.1 and 1 Hz and between 2 and 5 Hz received the greatest weight in determining the fit in the flat and sloping sections of the spectrum, respectively.

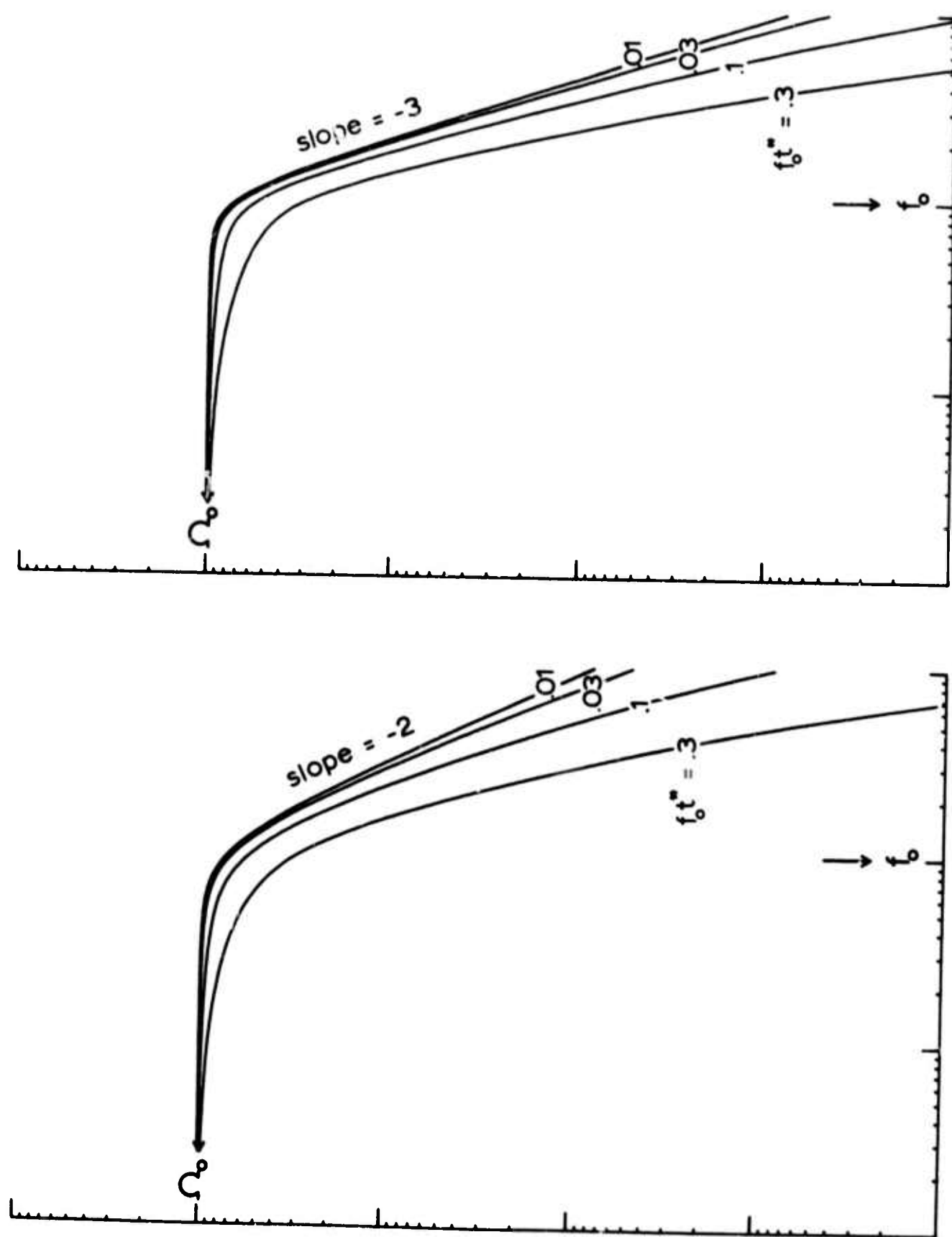


Figure 5. Templates used to obtain spectral estimates of the low-frequency level Ω_0 and the corner frequency f_0 for the cases where the high-frequency slope is -2 (left) and -3 (right) and for four values of t^* .

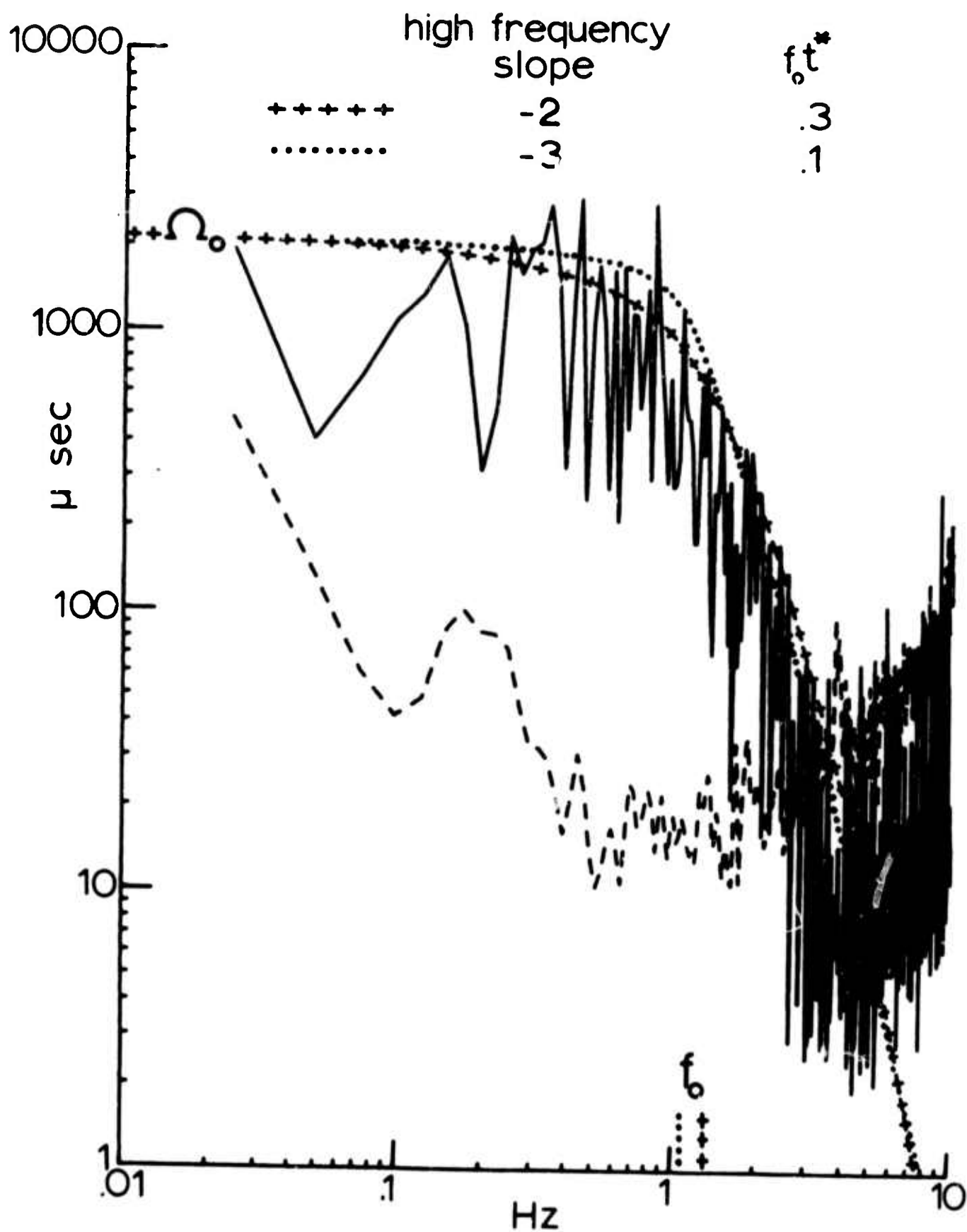


Figure 6. Example illustrating two different estimates of the low-frequency level Ω_0 and the corner frequency f_0 of the spectrum from the NS component at SAGO-East from event 6 (Table 1).

The method outlined above and illustrated in Figures 5 and 6 has the advantage of offering a uniform and systematic approach to the problem of estimating various spectral characteristics. It also illustrates some general limitations of the exercise. For instance, from a consideration of the parallel shape of the curves for various values of t^* in Figure 5 and the uneven nature of the observed spectra (Figures 4 and 6), it seems obvious that this method can not be used to determine t^* and thus Q . Hence t^* must be either known or assumed; but from the parallel shape of the curves in Figure 5 it is clear that the estimate of f_0 will be affected by the value used for t^* . The problem becomes even more indeterminant when one admits the possibility that the high-frequency slope is unknown and may vary from earthquake to earthquake. This is apparent in Figure 6 where the rate of high-frequency decay for a slope of -2 and a $f_0 t^*$ of 0.3 is about the same as for a slope of -3 and a $f_0 t^*$ of 0.1 over the frequency range available for fitting. In applying this method it was usually found that there were different combinations of slope and t^* which gave equally good fits to a particular spectrum. Most commonly the best fits involved slopes of -2 to -3 and t^* values of 0.1 to 0.3 sec. As can be seen in Figure 6 the estimate of the corner frequency f_0 is affected by the choice of the slope and t^* combination, with larger estimates of f_0 generally associated with the larger values of t^* . The approach followed in this study was to estimate Ω_0 and f_0 for all combinations of slope and t^* that gave good fits and then use the mean of these estimates. The scatter in the f_0 estimates about the mean was usually less than 30% while that in Ω_0 was usually less than 10%. The mean estimates of Ω_0 and f_0 are listed in Table 2 for each spectrum that was analyzed.

In addition to the conventional spectral studies described in the foregoing paragraphs, the data of this study afford the opportunity of studying the earthquake source in the time domain. Using the location and fault plane data in Table 1 and assuming a point dislocation imbedded in a halfspace as an earthquake model, it is possible to calculate synthetic seismograms (Johnson, 1974) which can be compared with the observed seismograms. While this model of the earthquake source is undoubtedly oversimplified, it does have the advantages of allowing an exact analytical calculation which includes both near-field and far-field terms and containing only two free parameters, the moment and rise time of the dislocation. These two parameters enter into the problem more or less independently, as the rise time is related to the width of the seismic pulse (and the corner frequency in the spectral domain) while the moment is related to the amplitude of the seismic pulse (and the low-frequency level in the spectral domain). Thus the synthetic seismograms provide an independent means of estimating some of the earthquake source parameters.

The velocity difference across the San Andreas fault zone (discussed earlier) was incorporated into the calculation of synthetic seismograms in an approximate manner by assuming the average P velocity of the halfspace to be 5.5 and 5.4 km/sec for paths to SAGO-Central and SAGO-East, respectively. The S velocity was inferred from the P velocity by assuming a value of 0.25 for Poisson's ratio, and the density was taken to be 2.67 gm/cm^3 . The time history of the dislocation was taken to be a step function with a finite rise time (time to reach the final dislocation value) such that the function and its first derivative are continuous everywhere (Lithiser, 1974). This means that the spectrum of the body waves radiated from this source will have a high-frequency slope of -2 in the far field.

The synthetic seismograms also provide a simple method of attacking a troublesome problem of near-field studies, the effect of tilts and spurious transients. All horizontal seismometers respond to tilts and at low frequencies the output of near-field seismometers resulting from ground tilt can be comparable to that resulting from ground displacement. There is no simple way of separating the two effects since horizontal acceleration due to tilt is indistinguishable from that due to horizontal displacement. However, synthetic seismograms due to ground tilt can be calculated in the same way as synthetic seismograms due to ground displacement and a comparison of the two gives a measure of the tilt effect for the source model used. The inference is then made that a similar effect may be present in the observed seismogram. This approach is rather qualitative but it has proved to be useful in analyzing the low frequencies in the observed spectra.

DISCUSSION

Table 2 is a summary of measurements obtained for the earthquakes listed in Table 1. Results are given for all components which recorded useable data from each earthquake. The maximum ground displacements are measures of maximum amplitude on displacement seismograms. Prior to this measurement the signals were filtered (2 Hz 1 pole low-pass) to remove high-frequency noise in the case of displacement transducers, and the signals were integrated in the case of velocity transducers. The spectral estimates of Ω_0 and f_0 were obtained with the method outlined in the previous section.

The low-frequency level Ω_0 was converted to an estimate of the seismic moment M_0 using the formula

$$M_0 = 4\pi\rho\beta^3R\Omega_0 \quad (1)$$

where ρ is the density, β is the S velocity of the medium, and R is the hypocentral distance. This formula assumes that Ω_0 is calculated from a far-field S wave, that the free surface effect can be ignored, and that the radiation pattern has no effect. Although none of these assumptions is strictly valid as used here, numerical experiments with whole-record spectra of synthetic seismograms from sources with known M_0 have indicated that this formula is reasonable for estimating the seismic moment with near-field data.

Consideration of the seismic moments listed in Table 2 shows that the values estimated at the SAGO-East site (located on Pliocene sediments) are always greater than those estimated at the SAGO-Central site (located on granite) for the same earthquake. On the average they differ by a factor of about 3. This difference is most likely due to the effect of geology at the recording site as it is seen for events in all source regions and appears to be independent of azimuth and distance to the earthquake. This observation of larger amplitudes on sediments than on basement rocks is fairly common in seismology (Gutenberg,

Table 2. Summary of measurements obtained from displacement seismograms and displacement spectra

Event	M_L	Component	Maximum ground displacement μ	Ω_0 μ -sec	f_0 Hz	$\log(M_0)$ dyne-cm
1	4.6	Central				
		NS	2847	1500	1.3	23.22
		EW	2918	930	1.4	23.01
		East				
		NS	3117	2600	1.4	23.43
		EW	3690	4000	1.2	23.61
2	4.7	Central				
		NS	329	337	1.7	22.60
		EW	751	430	1.7	22.71
		East				
		EW	2746	1500	2.1	23.15
3a	4.0	Central				
		NS	144	210	1.3	22.37
		EW	116	190	1.4	22.32
		East				
		NS	674	1500	1.6	23.27
		EW	456	690	1.6	22.93
3b	2.6	Central				
		NS	4	3	1.9	20.51
		EW	6	4	1.9	20.64
		Z	4	2	2.0	20.43
3c	3.7	Central				
		NS	90	150	1.1	22.19
		EW	90	130	1.1	22.13
		Z	59	75	1.2	21.89
3d	2.4	Central				
		NS	5	2	1.9	20.33
		EW	5	2	1.8	20.33
4a	5.1	Central				
		NS	1225	3000	1.0	23.87
		EW	1242	2700	1.0	23.82
		East				
		NS	2657	5500	1.4	24.14
		EW	3208	8000	1.2	24.31
4b	3.6	Central				
		NS	21	22	2.6	21.68
		EW	20	26	2.2	21.75
5	4.7	Central				
		NS	108	200	1.4	22.82
		EW	158	320	1.2	23.02
		Z	134	210	1.4	22.84

6	4.7	Central				
		NS	553	520	1.05	22.96
		EW	624	950	0.9	23.23
		East				
		NS	1292	2150	1.1	23.60
		EW	1087	2200	1.0	23.61
7a	4.9	Central				
		NS	1126	1600	1.2	23.11
		EW	1311	1200	1.3	22.98
		East				
		NS	4278	5900	1.3	23.76
		EW	2941	4500	1.3	23.64
7b	4.1	Central				
		NS	94	110	1.2	22.01
		EW	105	105	1.3	21.99
		Z	67	100	1.4	21.97
		East				
		NS	561	670	1.15	22.86
		EW	333	450	1.1	22.69
7c	3.0	Central				
		NS	12	13	1.8	21.13
		EW	9	10	1.8	21.01

1956a, 1956b, 1957), although one might expect the difference to vanish toward zero frequency. An alternative explanation is that the strong lateral contrast in crustal properties across the fault zone causes an asymmetric distribution in both stored and radiated elastic energy. This latter explanation would imply that studies of this type are capable of defining the absolute slip on each side of the fault.

Figure 7 shows $\log(M_0)$ from Table 2 plotted as a function of Wood-Anderson magnitude M_L . Each point represents the average $\log(M_0)$ obtained from the horizontal instruments at a given site. In constructing the plot the moments at SAGO-East were all divided by a factor of 3, so the plot can be considered appropriate for bedrock southwest of the San Andreas fault. The solid line was fit to the data points by linear regression analysis and has the equation

$$\log(M_0) = (17.60 \pm .28) + (1.16 \pm .06) M_L \quad (2)$$

The dashed line is the relation derived by Wyss and Brune (1968) for San Andreas earthquakes with magnitudes less than 6 and has the equation

$$\log(M_0) = 17.0 + 1.4 M_L \quad (3)$$

The main features of Figure 7 are the very linear log moment-magnitude relation and the good agreement between the data of this study and the results of Wyss and Brune (1968) in which the moments were estimated on the basis of surface wave amplitudes and field evidence. Both of these features support the contention of this paper that whole-record spectra of near-field seismograms yield reliable estimates of the seismic moment.

In the case of the corner frequencies f_0 listed in Table 2 there does not appear to be a systematic difference between the values estimated at SAGO-Central and SAGO-East for the same earthquake. Thus all estimates of f_0 for a given earthquake have been averaged in order to obtain the plots of $\log(f_0)$ versus both M_L and $\log(M_0)$ shown in Figure 8. Linear

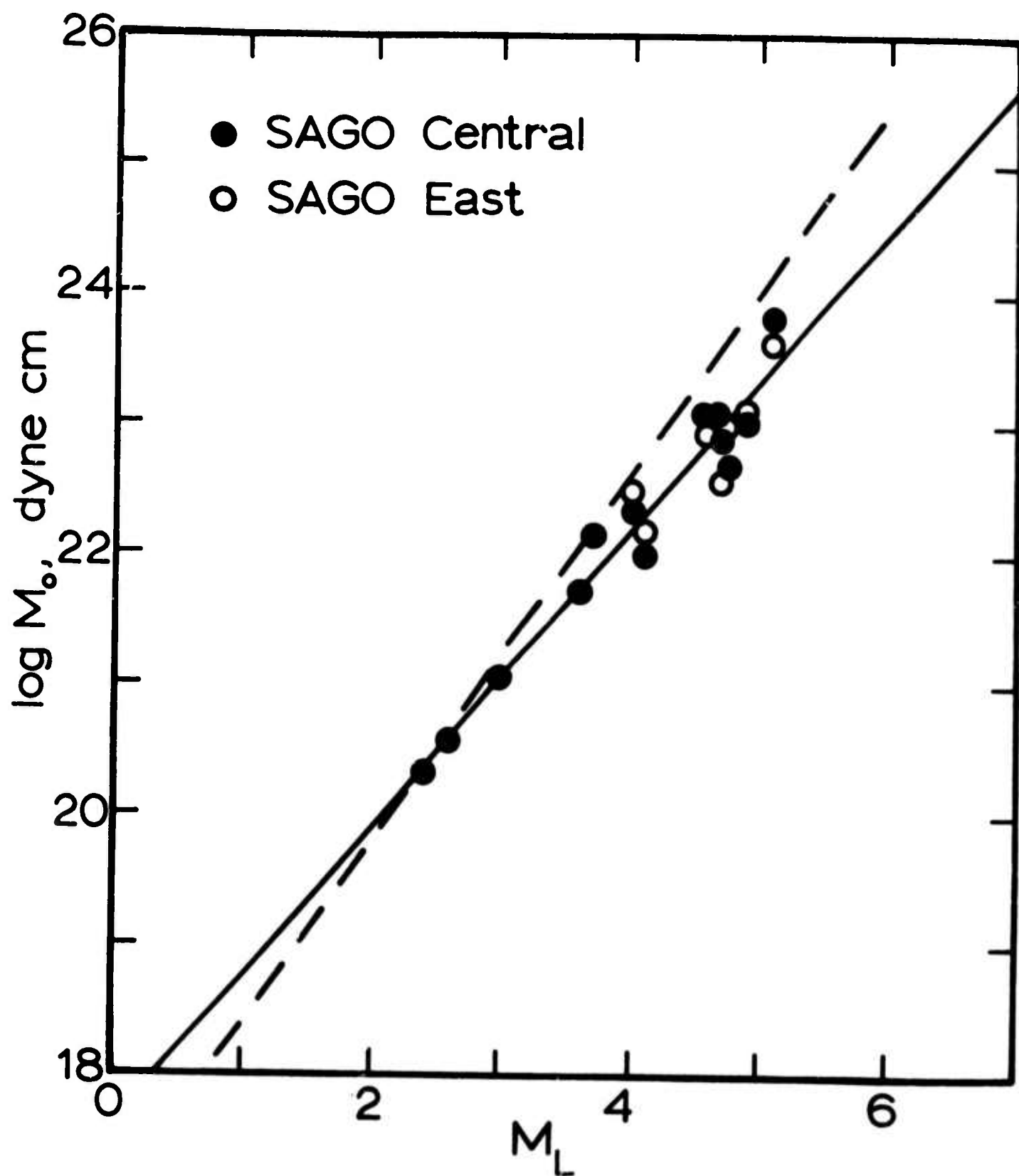


Figure 7. Relation between seismic moment and magnitude. The solid line was fit to the data points by linear regression and the dashed line is from Wyss and Brune (1968). The SAGO-East values have been divided by a factor of 3 to remove an amplification effect.

regression analysis of the data points in these plots yields the equations

$$\log(f_o) = (0.48 \pm .12) - (0.079 \pm .030) M_L \quad (4)$$

and

$$\log(f_o) = (1.80 \pm .52) - (0.073 \pm .023) \log(M_o) \quad (5)$$

The considerable scatter in the data points of Figure 8 is reflected in the rather large uncertainties associated with the slopes and intercepts of these least-squares lines. The present data do not allow any strong conclusions to be drawn concerning the existence of a systematic relation between f_o and either M_L or M_o . However, the general trend of the data points and the slopes of the regression lines in Figure 8 suggest that f_o is only weakly dependent upon either M_L or M_o for these central California earthquakes of small to moderate magnitude.

Considering now the individual earthquakes, it is convenient to begin with event number 1 which is the earthquake nearest to SAGO. The epicenter is east of the main trace of the San Andreas fault. On the basis of the compression axis indicated by the fault plane solution it appears to be associated with the Calaveras fault (Figure 1). Seismograms recorded from this earthquake (Figure 9) are fairly simple records, beginning with an emergent P wave and a gradually increasing disturbance interrupted by a large unipolar S pulse followed by a relatively small amplitude slowly decaying coda.

The dotted lines in Figure 9 are synthetic seismograms calculated for this earthquake according to the method outlined in the previous section. For the purposes of the calculation the fault plane solution given in Figure 2 and Table 1 was used but the epicenter was moved 1 km south from the location given in Table 1 in order to achieve agreement between the observed and calculated first motions of the P waves. This adjustment of 1 km is within

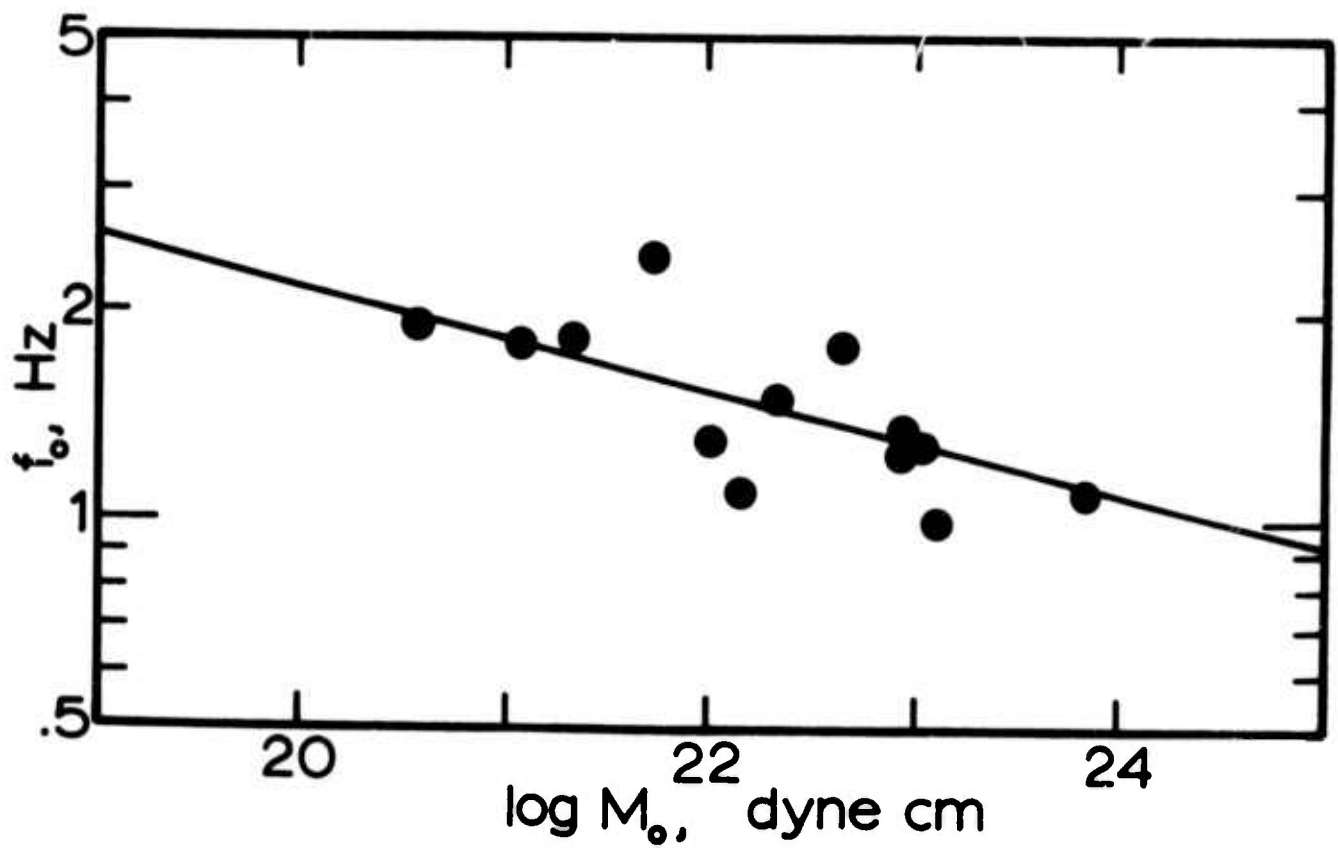
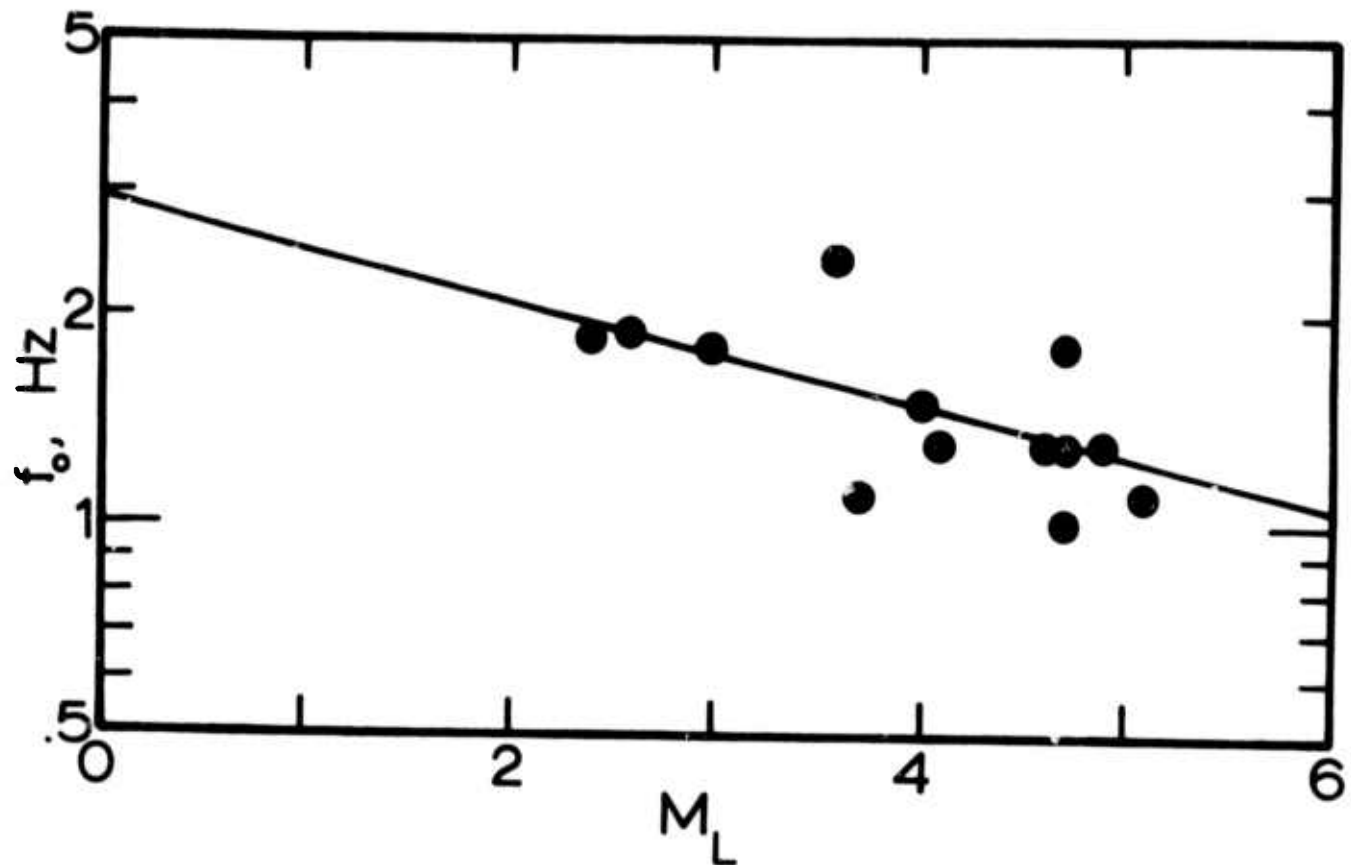


Figure 8. Relation between corner frequency and magnitude (top) and between corner frequency and log moment (bottom). In both graphs the line was fit to the data points by linear regression.

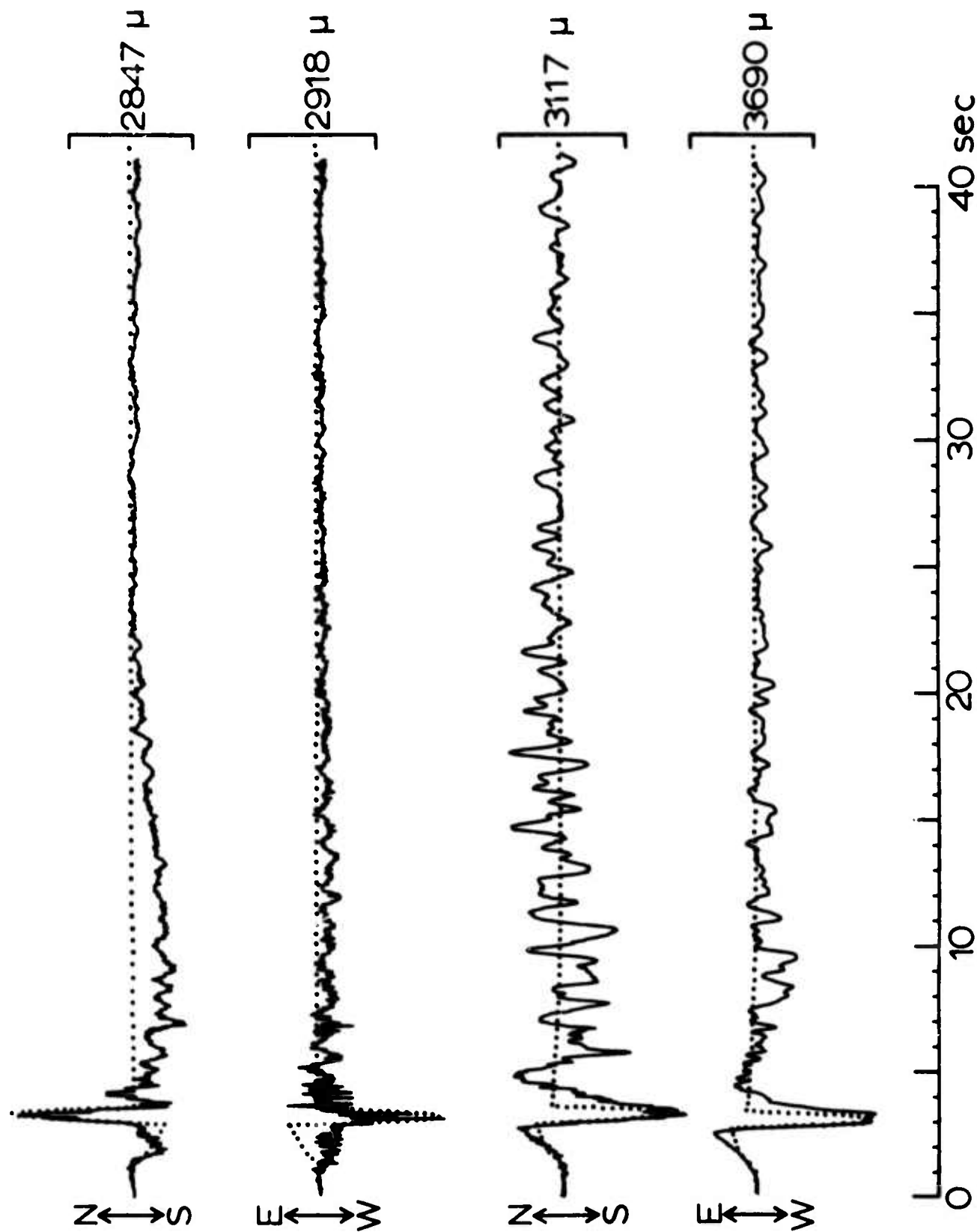


Figure 9. The displacement seismograms (solid lines) from event 1 (Table 1) recorded at SAGO-Central (top 2 traces) and at SAGO-East (bottom 2 traces). The dotted lines are synthetic seismograms calculated for this earthquake.

the uncertainty of the epicenter location. A rise time of 0.67 sec was used for the source function.

In their general features, the observed and synthetic seismograms in Figure 9 are fairly similar. First motions of the P waves are all in agreement, although it is difficult to see in the figure that the first motion on the EW synthetic seismogram at SAGO-Central is actually in the W direction. The S - P intervals are in agreement and the directions and shapes of the S pulses are quite similar. The portions of the seismograms between the beginnings of the P and S waves, which are mainly the contribution of the near-field parts of the solution, are in reasonable agreement at SAGO-East but at SAGO-Central there is an obvious discrepancy which has not yet been explained. Because the synthetic seismograms were calculated for a homogeneous halfspace, they are incapable of matching the coda that follows the S pulse on the observed seismograms.

The major features on both the observed and synthetic seismograms are the S pulses. Note that, just as in far-field calculations, the shape of the S pulse on the synthetic seismograms is essentially the derivative of the source time function. The duration of the S pulse can thus be interpreted as an estimate of the rise time of the source function. At SAGO-Central the duration of the observed and synthetic S pulses are in good agreement. At SAGO-East it appears that the agreement could be considerably improved if the rise time were increased from 0.67 sec to about 1.0 sec, but such a change would destroy the agreement at SAGO-Central and it would also degrade the fit between the observed and synthetic spectra (Figure 10). An hypothesis that attributes the increased duration of the S pulse at SAGO-East to the superposition of two or more S pulses seems to be the most reasonable explanation at the present time. A major discontinuity, the San Andreas

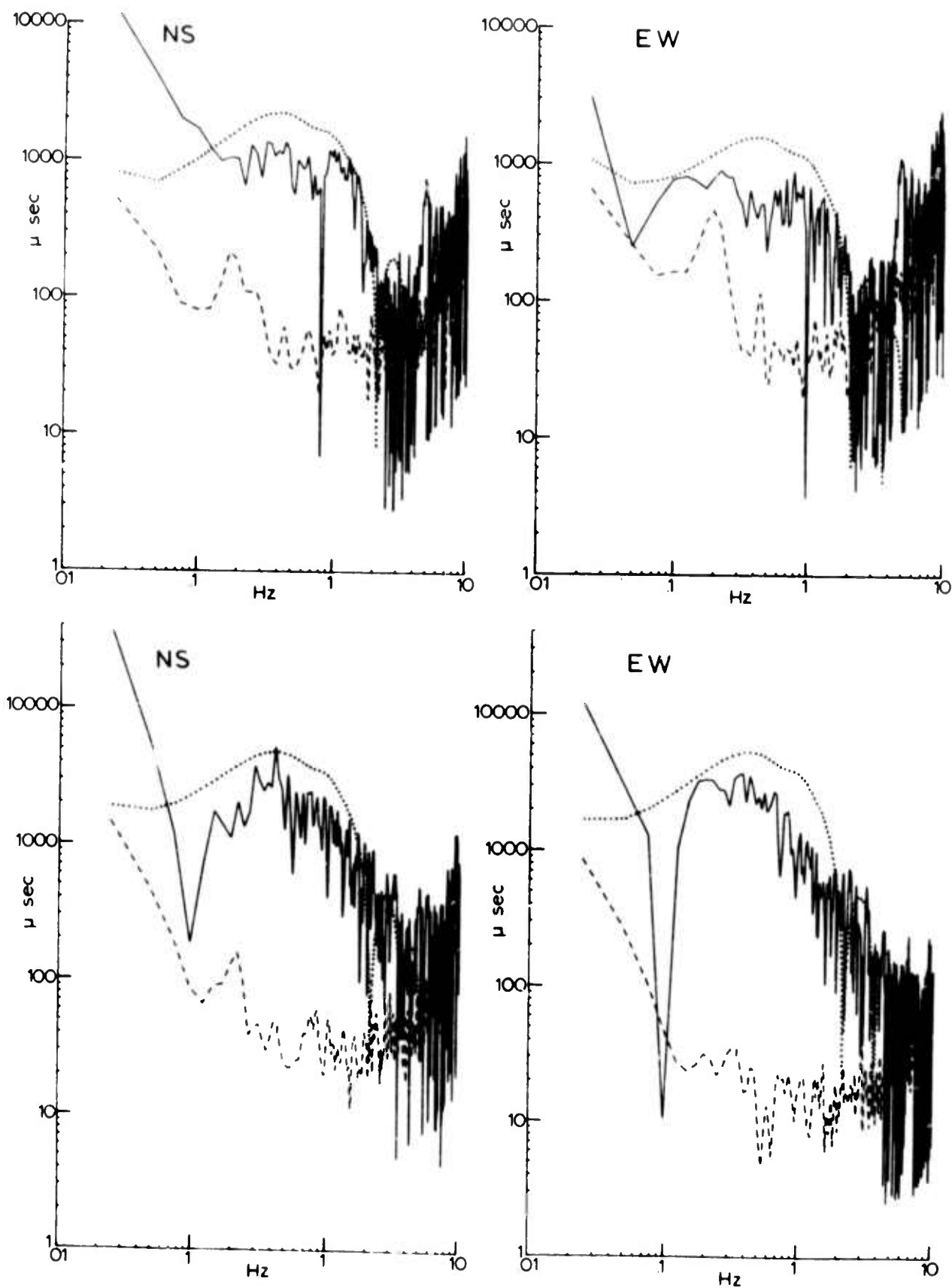


Figure 10. Amplitude density spectra calculated for event 1 (Table 1) from seismograms (Figure 9) recorded at SAGO-Central (top 2 spectra) and at SAGO-East (bottom 2 spectra). The solid lines are calculated from the observed seismograms, the dashed lines are estimates of the noise, and the dotted lines are calculated from the synthetic seismograms.

fault, lies between the two stations and may be responsible for such an effect.

The synthetic seismograms provide a means of estimating the source moment from a consideration of the time domain alone. The estimate is obtained by adjusting the source moment of the synthetic earthquake until the amplitude of the S pulse on the synthetic seismogram matches that on the observed seismogram. Such time-domain estimates of the moment were obtained for each component of recorded ground motion and the results are listed in Table 3.

The spectra computed from the seismograms of Figure 9 are shown in Figure 10. They illustrate another method of estimating the seismic source moment. In this case the moment of the synthetic earthquake is adjusted until the synthetic spectrum is a reasonable fit to the observed spectrum. Such frequency-domain estimates of the moment were obtained for each component of recorded ground motion and the results are listed in Table 3.

Note that the effects of radiation pattern, free surface, and propagation are all incorporated when the synthetic calculations are used to estimate the seismic moment in either the time domain or frequency domain. The radiation pattern is particularly important for event 1 because it is a strike-slip earthquake located almost directly below the recording stations, and thus it is not surprising that the moment estimates in Table 3 are greater than those in Table 2 which were obtained without regard for the effects of the radiation pattern. Also note that the effect of attenuation has not been included in the synthetic calculations, although it could be done given an appropriate value of Q .

An interesting feature of the spectra in Figure 10 deserving further attention is the rise in the observed spectra toward the low frequencies. The synthetic spectra do not show this feature. A possible explanation

Table 3. Seismic moments determined with the aid of synthetic seismograms

Event	M_L	Rise Time sec	Component	Time Domain $\log(M_0)$ dyne-cm	Frequency Domain $\log(M_0)$ dyne-cm
1	4.6	0.67	Central		
			NS	23.51	23.67
			EW	23.47	23.65
			East		
			NS	23.83	24.30
			EW	23.76	24.19
2	4.7	0.50	Central		
			NS	22.83	23.05
			EW	22.54	22.77
			East		
			EW	23.18	23.48
4a	5.1	1.00	Central		
			NS	23.19	23.67
			EW	23.25	23.81
			East		
			NS	23.66	24.16
			EW	23.62	24.17
7a	4.9	0.67	Central		
			NS	22.65	23.06
			EW	22.95	23.03
			East		
			NS	22.69	23.53
			EW	23.25	23.82

of this difference involves the tilts associated with the seismic waves which appear as apparent accelerations to the horizontal seismometers. As a check on this possibility the synthetic seismograms resulting from elastic tilts were calculated and are shown in Figure 11. The total synthetic seismogram can thus be obtained by adding these tilt-induced records to the synthetic records resulting from displacements (dotted lines in Figure 9). The primary effect of the tilts, which retain static values after passage of the waves, is permanent offsets on the seismograms. In this particular case, however, the offsets are small compared to the maximum displacements and have a very small effect upon the synthetic spectra. While synthetic tilts calculated for an elastic halfspace model are too small to explain the discrepancy between the observed and synthetic spectra, it is possible that the use of a more realistic model with vertical inhomogeneities could lead to an amplification of the synthetic tilts. However, regardless of the model employed, the primary effect of the elastic tilts will undoubtedly be permanent offsets on the seismograms, and an inspection of the observed seismograms in Figure 9 indicates that this is not likely to be the required solution.

The primary discrepancy between the observed and synthetic seismograms in Figure 9 is a long-period transient feature in the observed seismograms that reaches a maximum some 5 to 10 sec after the S wave. The shape of this feature, which is best displayed on the NS component at SAGO-Central, suggests that it could be explained as the instrumental response to an impulse in tilt. This is confirmed in Figure 12 which is identical to Figure 9 except that the response due to an impulse in tilt has been added to the synthetic seismograms. The impulse in tilt was assumed to occur at the arrival time of the S wave, had a duration of 0.67 sec,

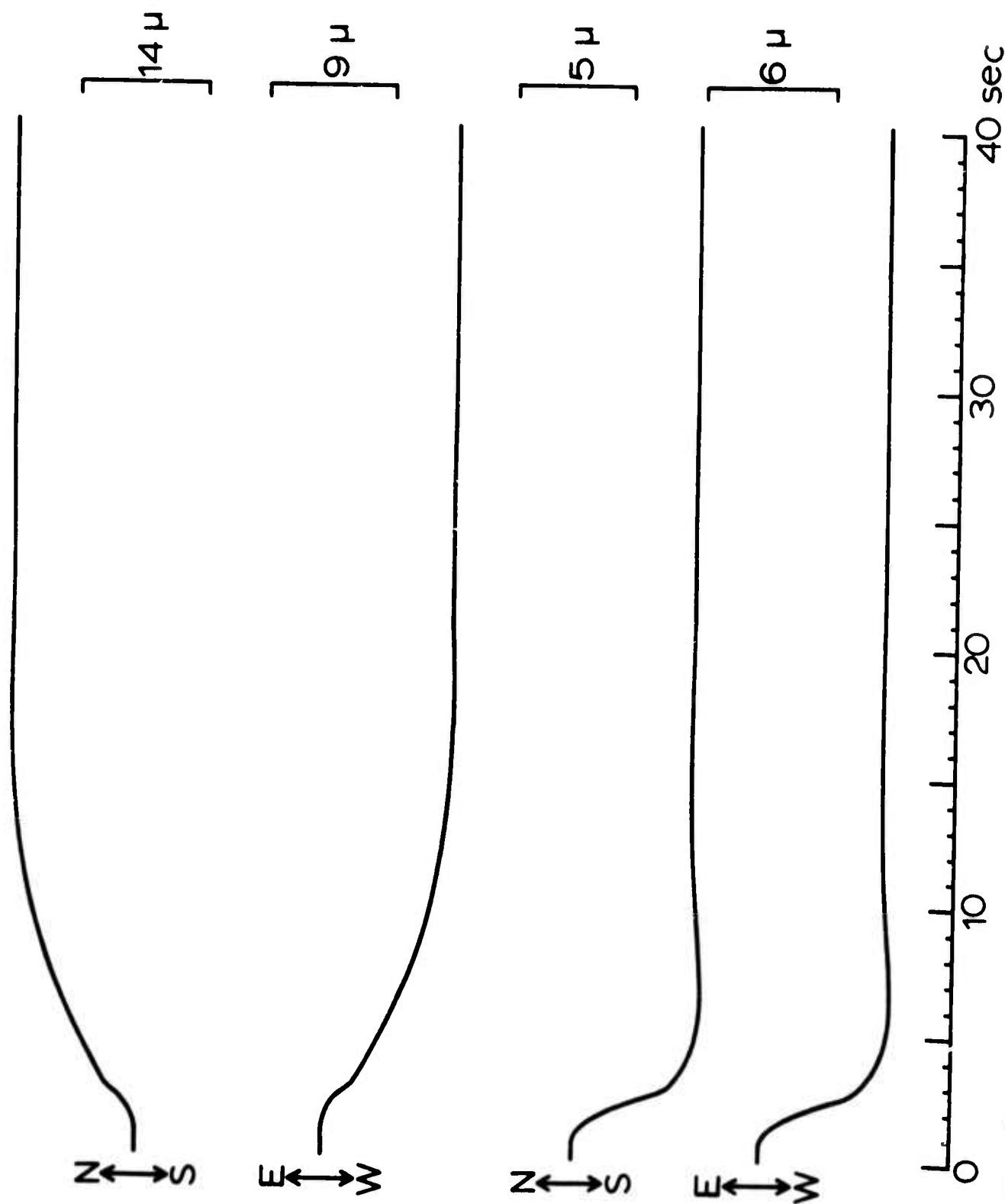


Figure 11. The predicted outputs of the displacement seismographs at SAGO-Central (top 2 traces) and at SAGO-East (bottom 2 traces) due to the elastic tilts calculated for event 1 (Table 1). The amplitudes on the right are equivalent ground displacements. The earthquake model used in this calculation is identical to that used for the synthetic results in Figures 9 and 10.

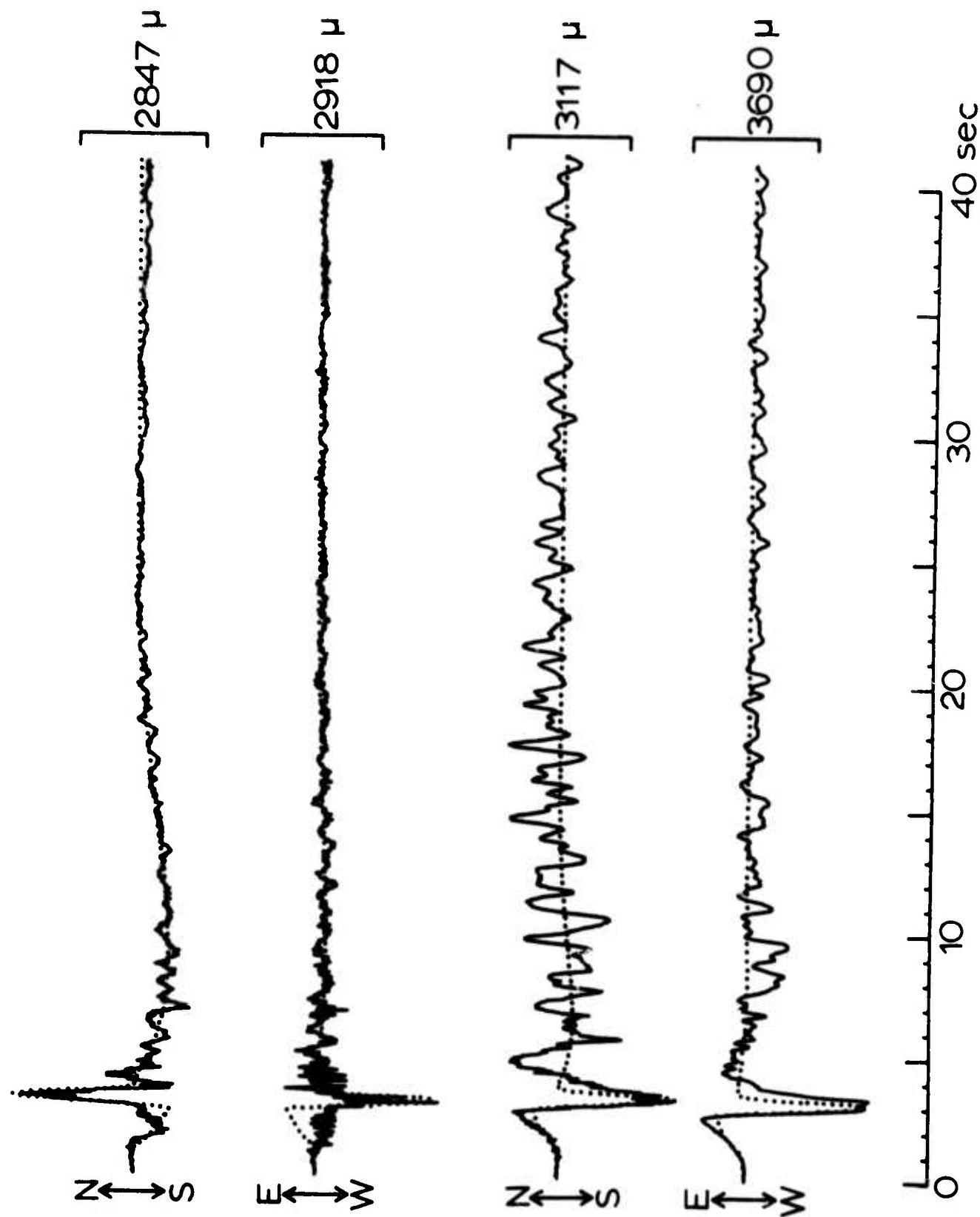


Figure 12. The displacement seismograms from event 1 (Table 1) recorded at SACO-Central (top 2 traces) and at SACO-East (bottom 2 traces). The dotted lines are the synthetic seismograms of Figure 9 with an additional negative impulse in tilt at the arrival time of the S wave.

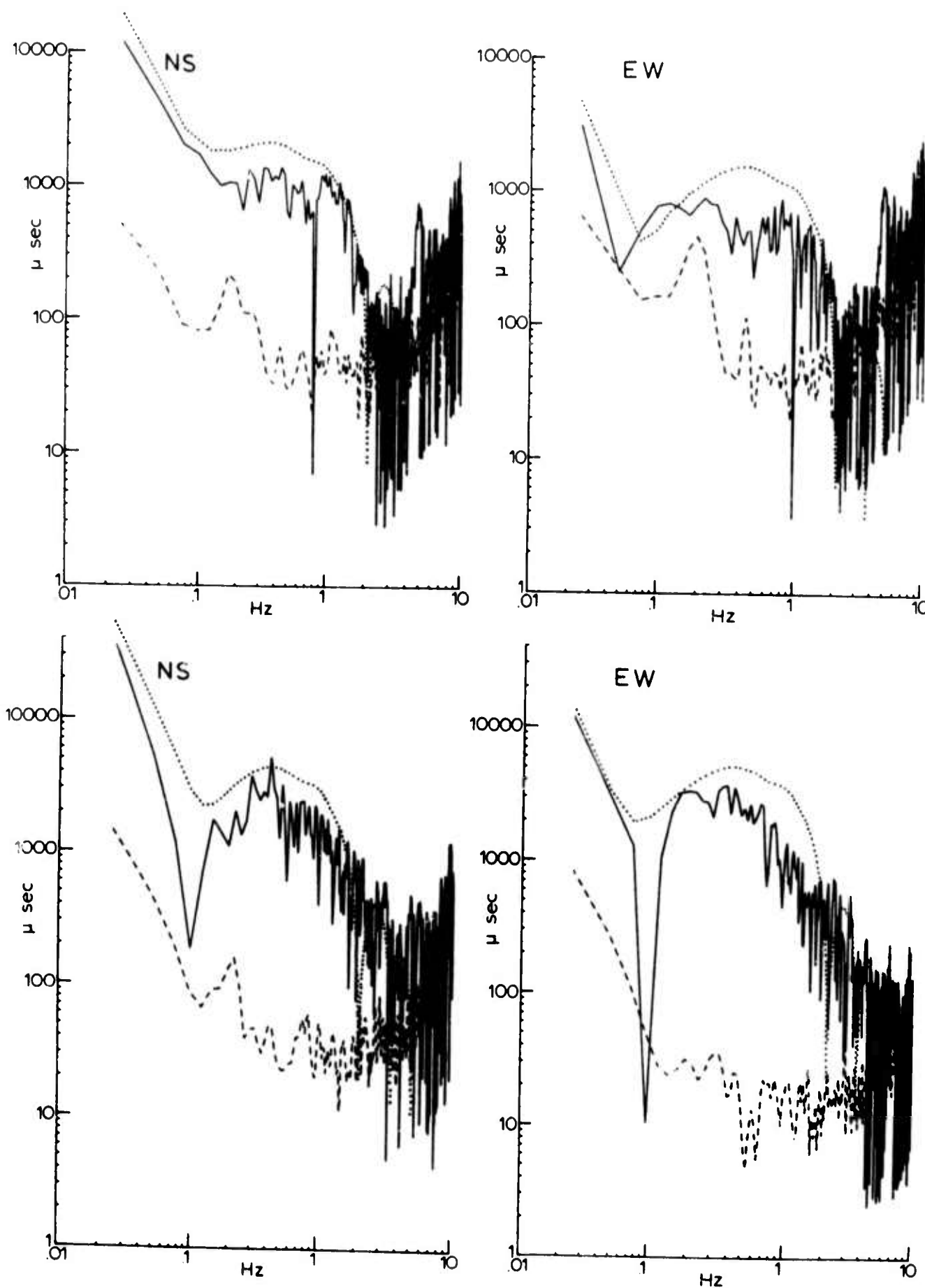


Figure 13. Amplitude density spectra calculated for event 1 (Table 1). The solid and dashed lines are identical to those of Figure 10 but the dotted lines are calculated from the synthetic seismograms of Figure 12 which include the effects of an impulse in tilt.

and had amplitudes of -87, -20, -104, and -29 micro-radians on the components SAGO-Central NS, EW, SAGO-East NS, and EW, respectively. The spectra are given in Figure 13. Comparing Figures 12 and 13 with 9 and 10 shows that an impulse in tilt is capable of explaining the discrepancy between the observed and synthetic seismograms. But the cause of such an impulse is not explained by this exercise and a number of possibilities exist. The possibility that it is a direct effect of the earthquake source which was not included in our simple synthetic model seems unlikely, but it can not be completely ruled out. The possibility of a nonlinear instrumental effect such as a rocking, sliding, or flexing of the instruments during the strong ground motion of the earthquake seems more likely. In any case, it is clear that considerable care must be taken with the interpretation of near-field spectra at low frequencies.

The seismograms and spectra for event number 2 are shown in Figures 14 and 15, respectively. This earthquake is apparently associated with the Calaveras fault (Figure 1). The NS component at SAGO-East did not provide a useable seismogram from this earthquake because the pendulum was too near one of the stops to record the ground motion which was several mm in amplitude. Synthetic seismograms were calculated and used to estimate the time-domain and frequency-domain seismic moments listed in Table 3. A rise time of 0.50 sec was assumed for the source function. The agreement between the observed and synthetic seismograms is reasonable up through the arrival of the S pulse. Note that at SAGO-Central the epicentral distance is slightly greater than the source depth, and in this circumstance the SV wave that appears on the NS component is quite different in appearance from the SH wave that appears on the EW component. The agreement between

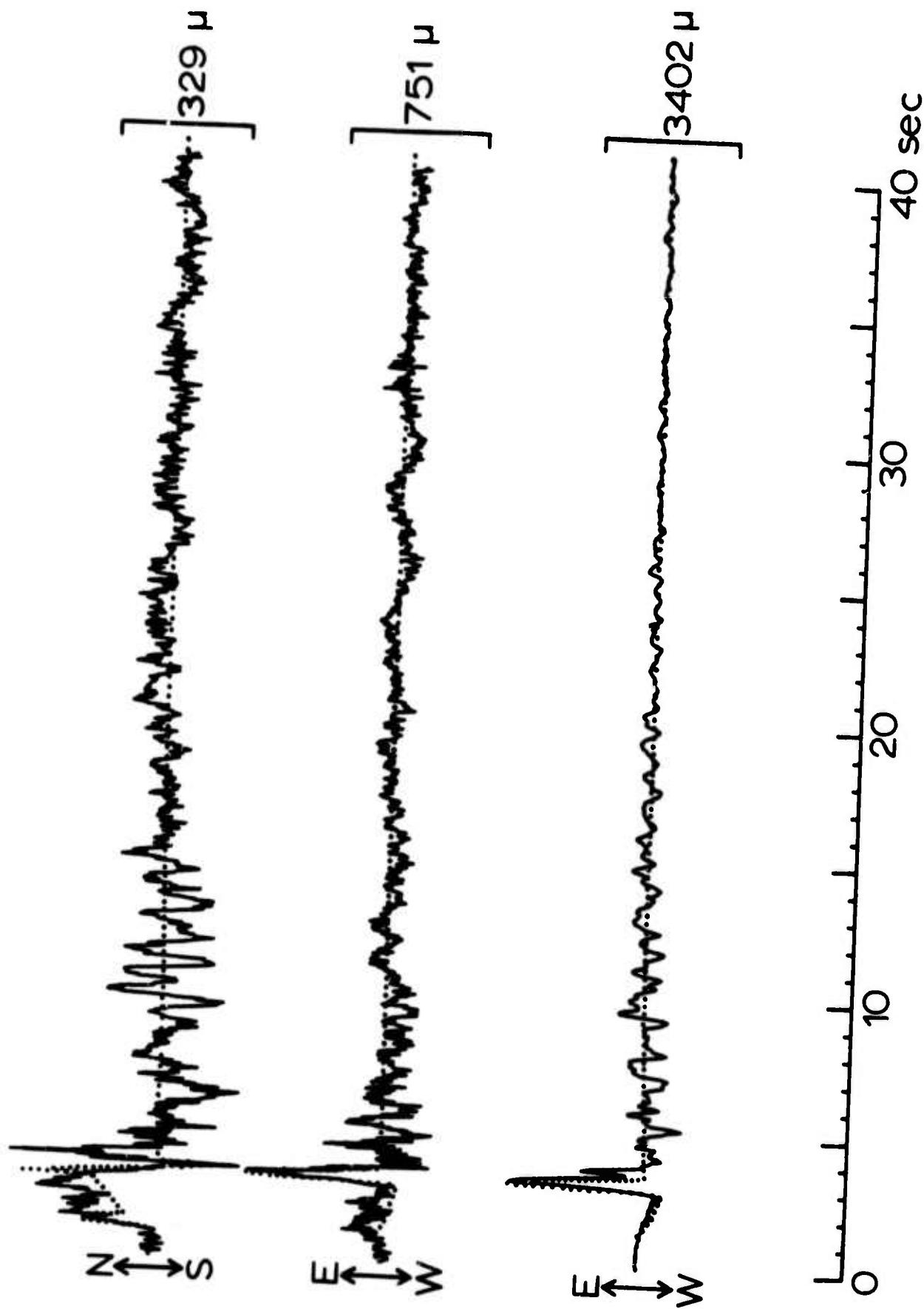


Figure 14. The displacement seismograms (solid lines) from event 2 (Table 1) recorded at SAGO-Central (top 2 traces) and at SAGO-East (bottom trace). The dotted lines are synthetic seismograms calculated for this earthquake.

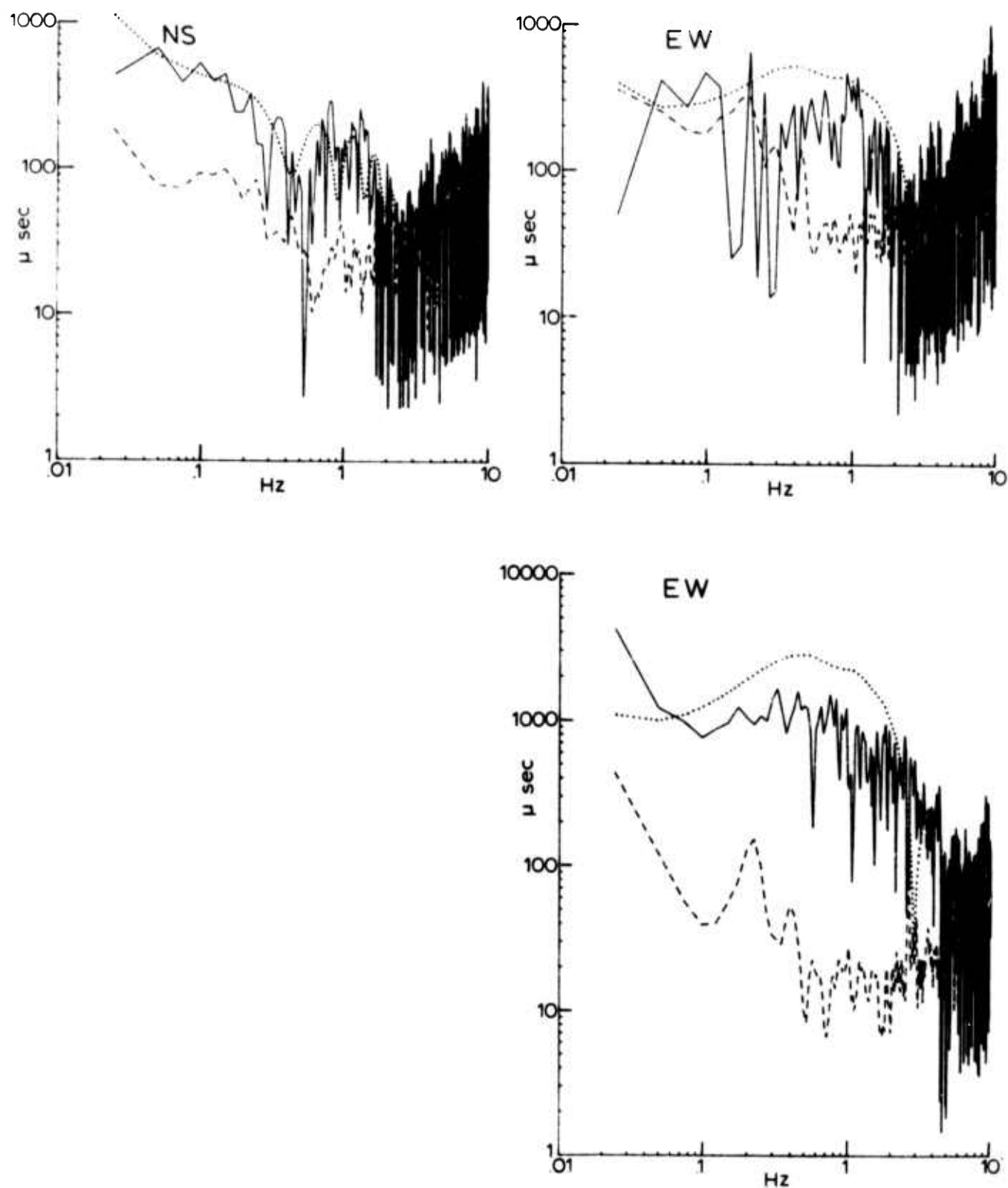


Figure 15. Amplitude density spectra calculated for event 2 (Table 1) from seismograms (Figure 14) recorded at SAGO-Central (top 2 spectra) and at SAGO-East (bottom spectrum). The solid lines are calculated from the observed seismograms, the dashed lines are estimates of the noise, and the dotted lines are calculated from the synthetic seismograms.

the observed and synthetic spectra is also reasonable, although the noise level at SAGO-Central is large enough to obscure much of the high-frequency behavior.

The seismograms and spectra for event number 7a are shown in Figures 16 and 17, respectively. In terms of both location (Figure 1) and fault plane solution (Figure 2) this earthquake appears to be associated with the Pinecate-Vergeles fault complex to the west of the main trace of the San Andreas fault. Synthetic seismograms and spectra calculated on the basis of this location and fault plane solution and a rise time of 0.67 sec are also shown in the figures and were used to calculate the time-domain and frequency-domain seismic moments listed in Table 3. In terms of general features the observed and synthetic results are in fair agreement. The comparison between observed and synthetic seismograms at SAGO-Central indicates that the waves have approached the station from a more northerly direction than implied by the synthetic calculations, and this could arise from either a small inaccuracy in the epicenter location or curvature in the wave paths due to velocity inhomogeneity. At SAGO-East the largest amplitudes on the seismograms occur several seconds after the arrival of the S waves. This unusually large coda may be associated with the fact that in travelling to SAGO-East the waves have passed from material with higher velocity and lower vertical velocity gradient west of the San Andreas fault into material with lower velocity and higher vertical velocity gradient east of the fault. Note however, that this phenomenon does not appear when the waves cross the fault in the other direction as in the case of the seismograms recorded at SAGO-Central from events 1 and 2 (Figures 9 and 14).

Another interesting aspect of this earthquake is the fact that the rise time of 0.67 sec which gives a reasonable fit between the observed and synthetic spectra (Figure 17) is too short to explain the duration

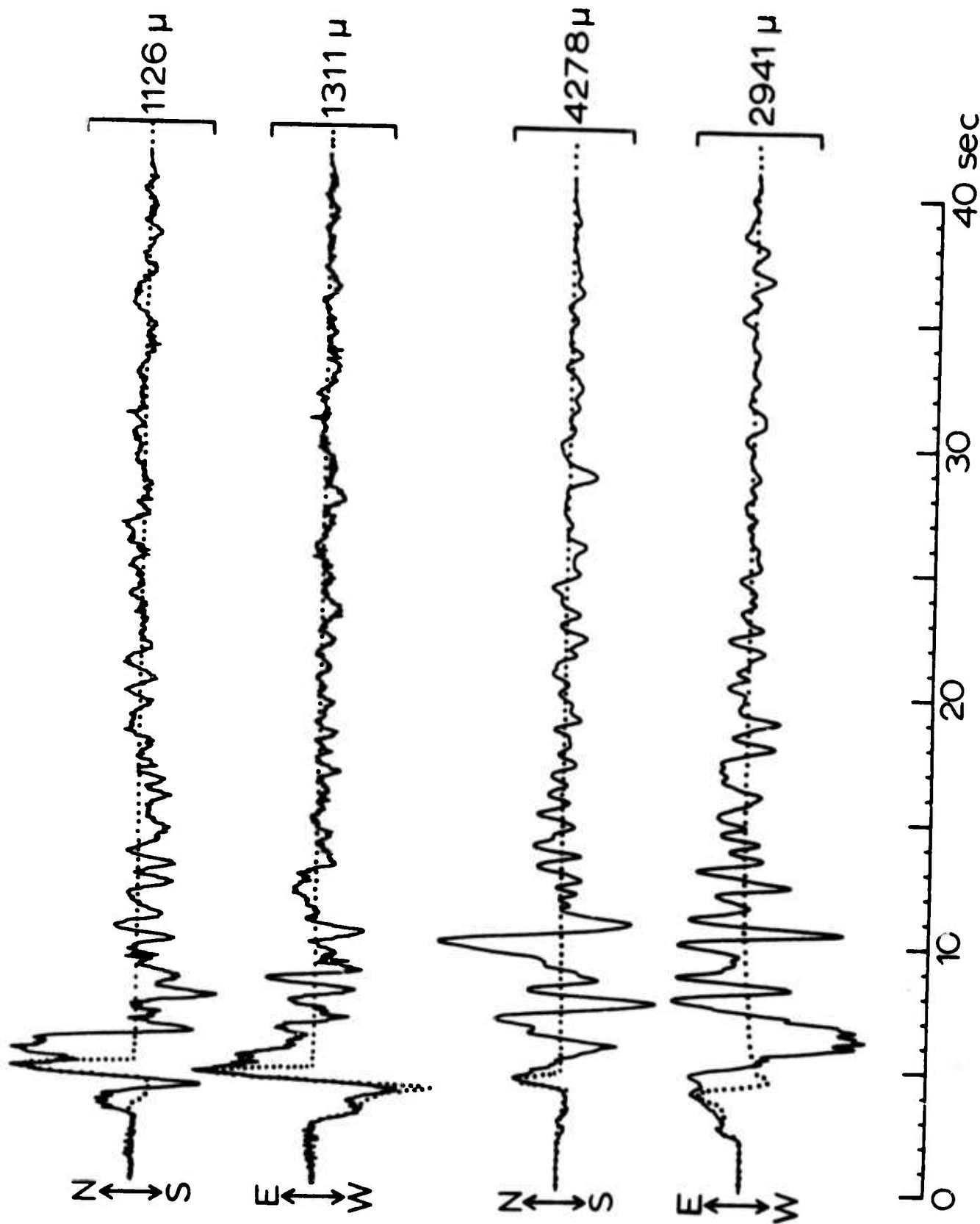


Figure 16. The displacement seismograms (solid lines) from event 7a (Table 1) recorded at SAGO-Central (top 2 traces) and at SAGO-East (bottom 2 traces). The dotted lines are synthetic seismograms calculated for this earthquake.

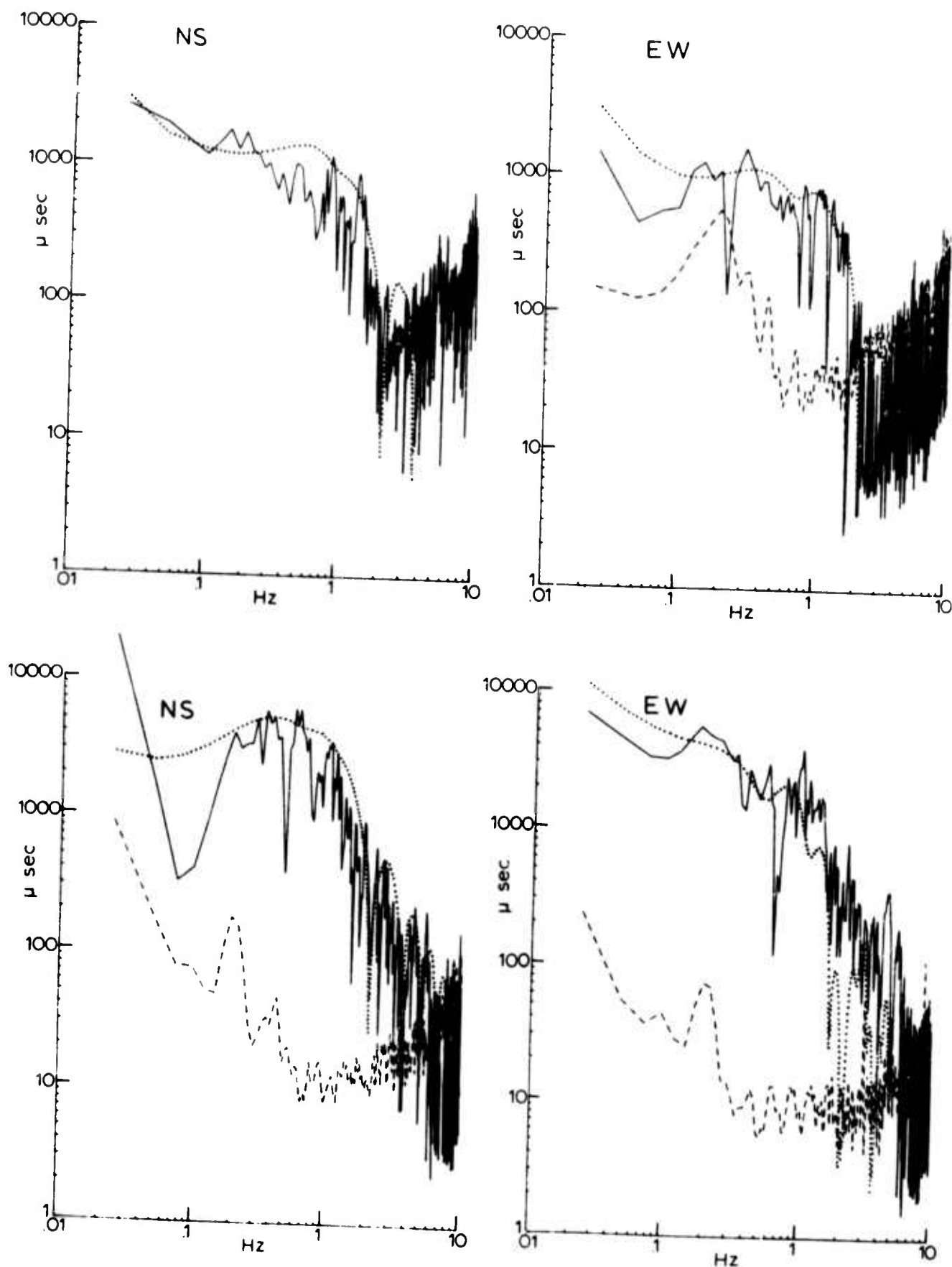


Figure 17. Amplitude density spectra calculated for event 7a (Table 1) from seismograms (Figure 16) recorded at SAGO-Central (top 2 spectra) and at SAGO-East (bottom 2 spectra). The solid lines are calculated from the observed seismograms, the dashed lines are estimates of the noise, and the dotted lines are calculated from the synthetic seismograms.

of the large S pulse. This is best observed on the SAGO-Central recordings in Figure 16, and a similar situation exists on the SAGO-East seismograms from events 1 (Figure 9) and 2 (Figure 14). As mentioned earlier, it appears as if the S pulse actually consists of the superposition of two or more pulses. Calling upon some source-related phenomenon such as finite source size to explain these features seems reasonable, but such a hypothesis is challenged by the results shown in Figure 18. This figure compares the seismograms recorded at SAGO-Central from event 7a with those recorded from two other earthquakes in the same source region, events 7b and 7c. The important point is that, even though these 3 earthquakes cover a magnitude range of almost 2, the seismograms have a very similar appearance. The length of the S pulse does not show an obvious dependence upon the magnitude of the earthquake, which argues against it being caused by the source itself. An alternate explanation which seems more acceptable at the present time would attribute the multiple nature of the S pulse to wave propagation effects due to inhomogeneities along the path between the earthquake and seismometer.

Next consider event number 4a for which the seismograms and spectra are shown in Figures 19 and 20, respectively. The synthetic results in these figures were calculated assuming a rise time of 1.0 sec for the source function. The fault plane solution for this earthquake gave a strike of N55W for the fault plane (Table 1). However, in order to explain the first motions of the P waves a strike of N45W, which coincides with the strike of the San Andreas fault in this region, was used in the synthetic calculations. Comparison of the observed and synthetic seismograms in Figure 19 shows considerable contrast between SAGO-Central and SAGO-East in spite of the fact that both stations are at approximately the same distance and azimuth

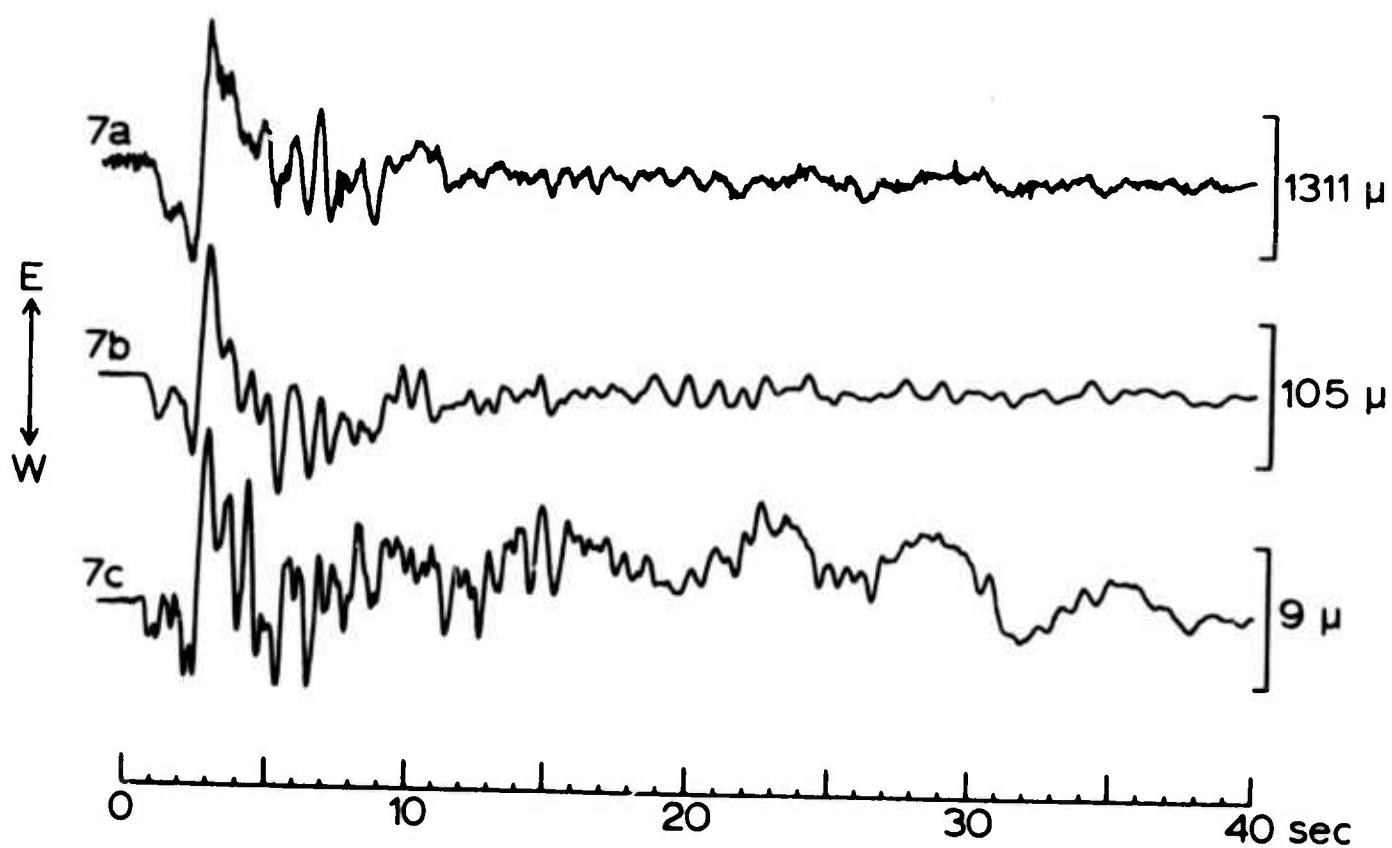
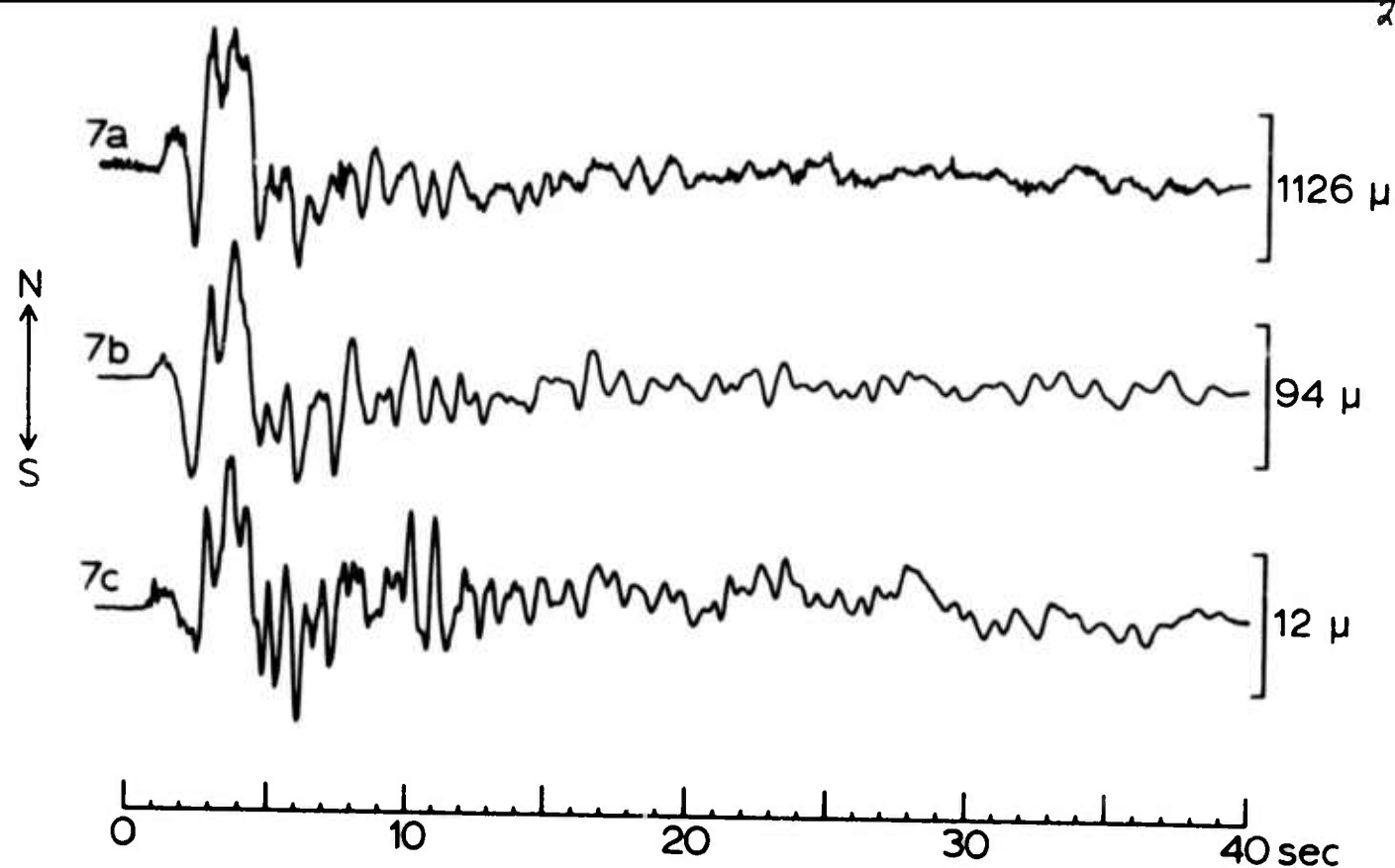


Figure 18. The displacement seismograms recorded at SAGO-Central from event 7a, 7b, and 7c (Table 1) with magnitudes 4.9, 4.1, and 3.0, respectively.

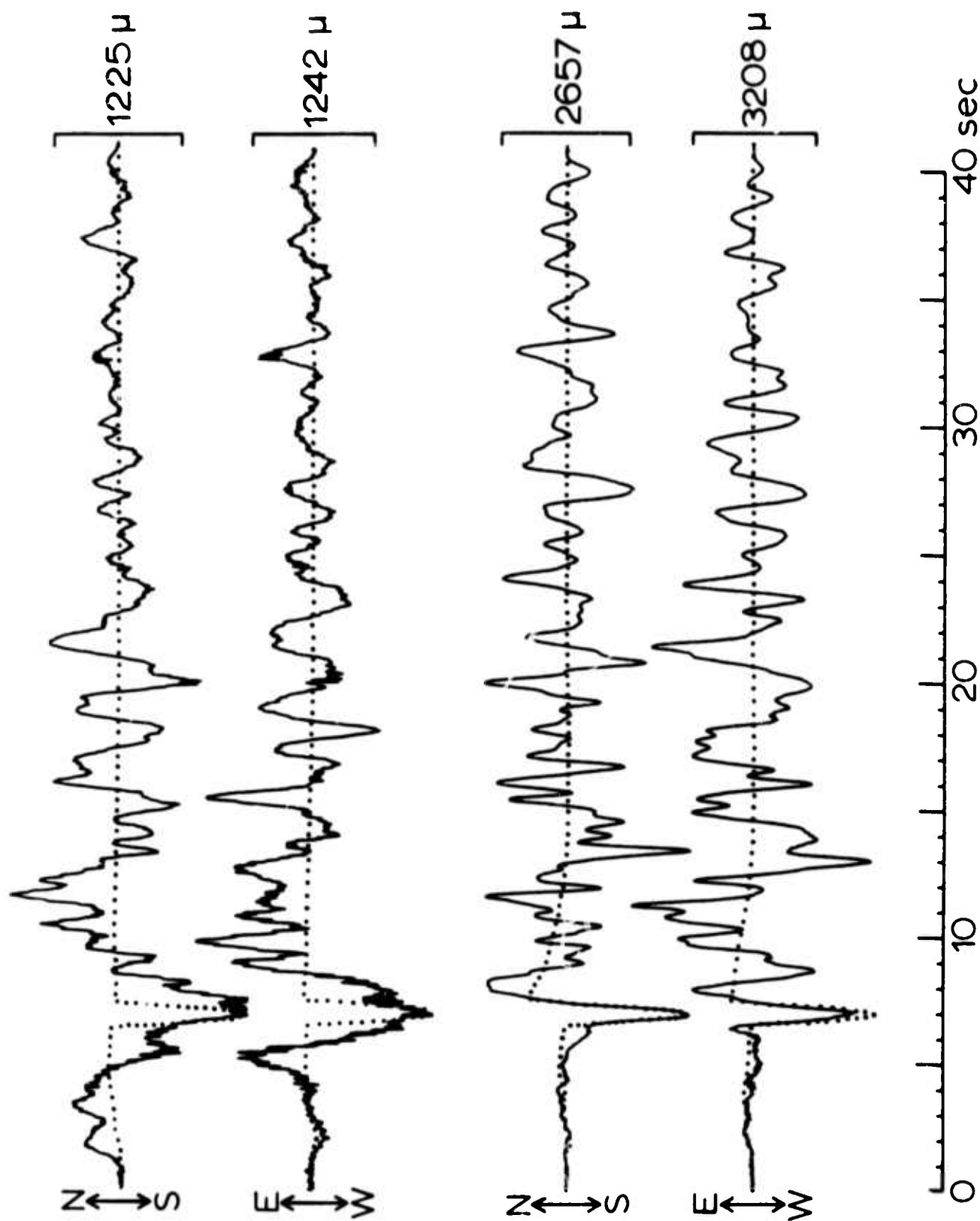


Figure 19. The displacement seismograms (solid lines) from event 4a (Table 1) recorded at SAGO-Central (top 2 traces) and at SAGO-East (bottom 2 traces). The dotted lines are synthetic seismograms calculated for this earthquake.

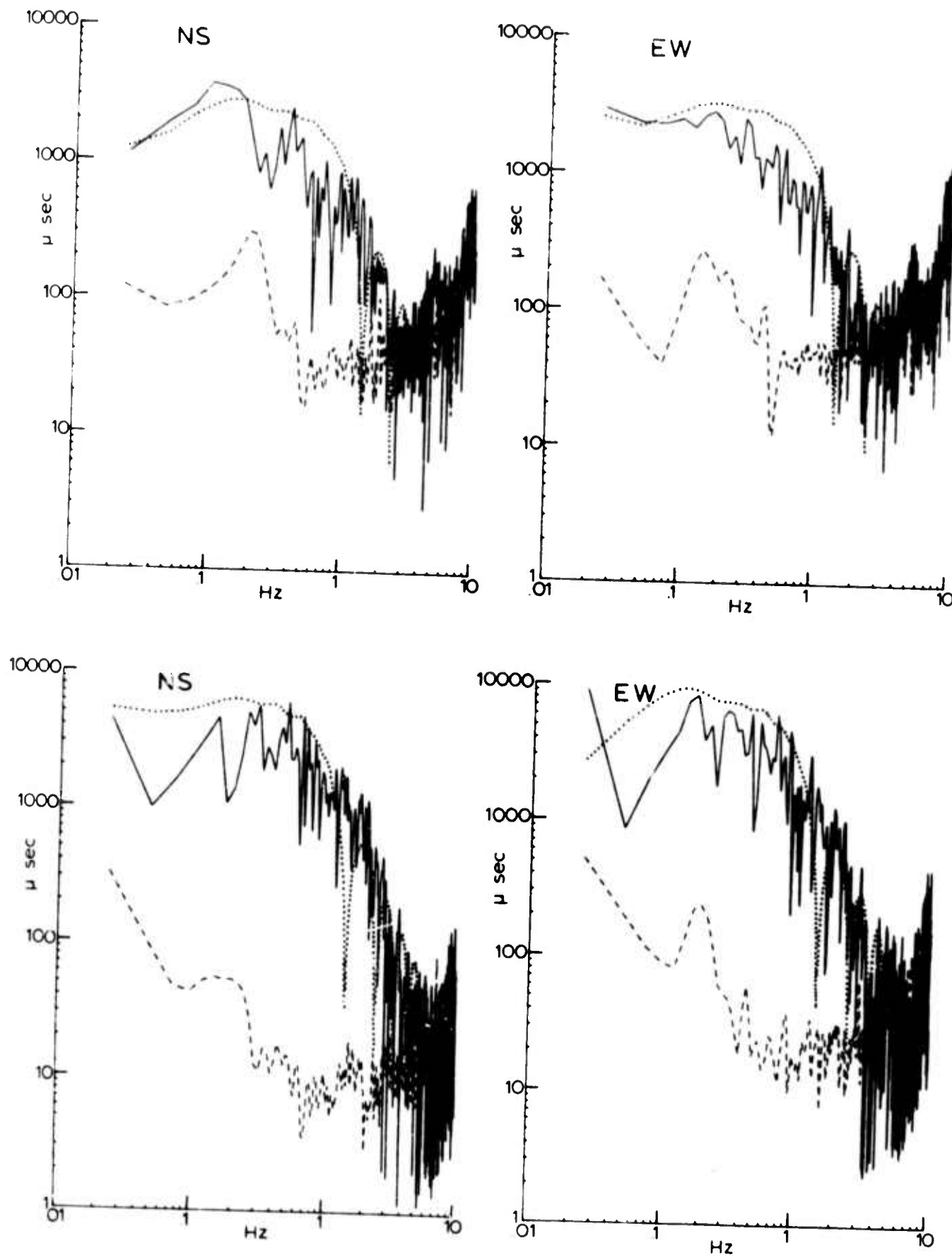


Figure 20. Amplitude density spectra calculated for event 4a (Table 1) from seismograms (Figure 19) recorded at SAGO-Central (top 2 spectra) and at SAGO-East (bottom 2 spectra). The solid lines are calculated from the observed seismograms, the dashed lines are estimates of the noise, and the dotted lines are calculated from the synthetic seismograms

from the earthquake (Table 1). At SAGO-East the observed and synthetic seismograms are in good agreement up through the arrival time of the S pulse, whereas at SAGO-Central there is little similarity in the records aside from the polarity of the P and S waves. Note however, that even in the case of SAGO-Central the observed and synthetic spectra agree quite well (Figure 20), and this again leads to the interpretation that the long duration of the S pulse on the observed seismograms at SAGO-Central is caused by a superposition of several shorter pulses.

Because the synthetic seismograms in this paper were calculated for a homogeneous halfspace, they do not contain a coda such as appears on the observed seismograms. This coda is often small (Figures 9, 14, and 16) but for event number 4a (Figure 19) it accounts for a significant fraction of the energy on the seismogram. It is usually assumed that this coda is caused by vertical or lateral inhomogeneities in the structure of the crust. Figure 21 is of interest in this respect because it illustrates the effect of epicentral distance upon the seismogram. In this figure are the seismograms recorded at SAGO-East from events 4a, 6, and 3a, which are similar earthquakes in all respects except for the epicentral distances. Note that, aside from a change in the S - P interval which is difficult to see in this figure, the seismograms are nearly identical through the arrival of the S pulse and 5 to 10 sec into the coda. This observation of a well developed and coherent coda for these earthquakes suggests that an investigation of the developing surface wave train in the near field may provide information on source parameters such as depth.

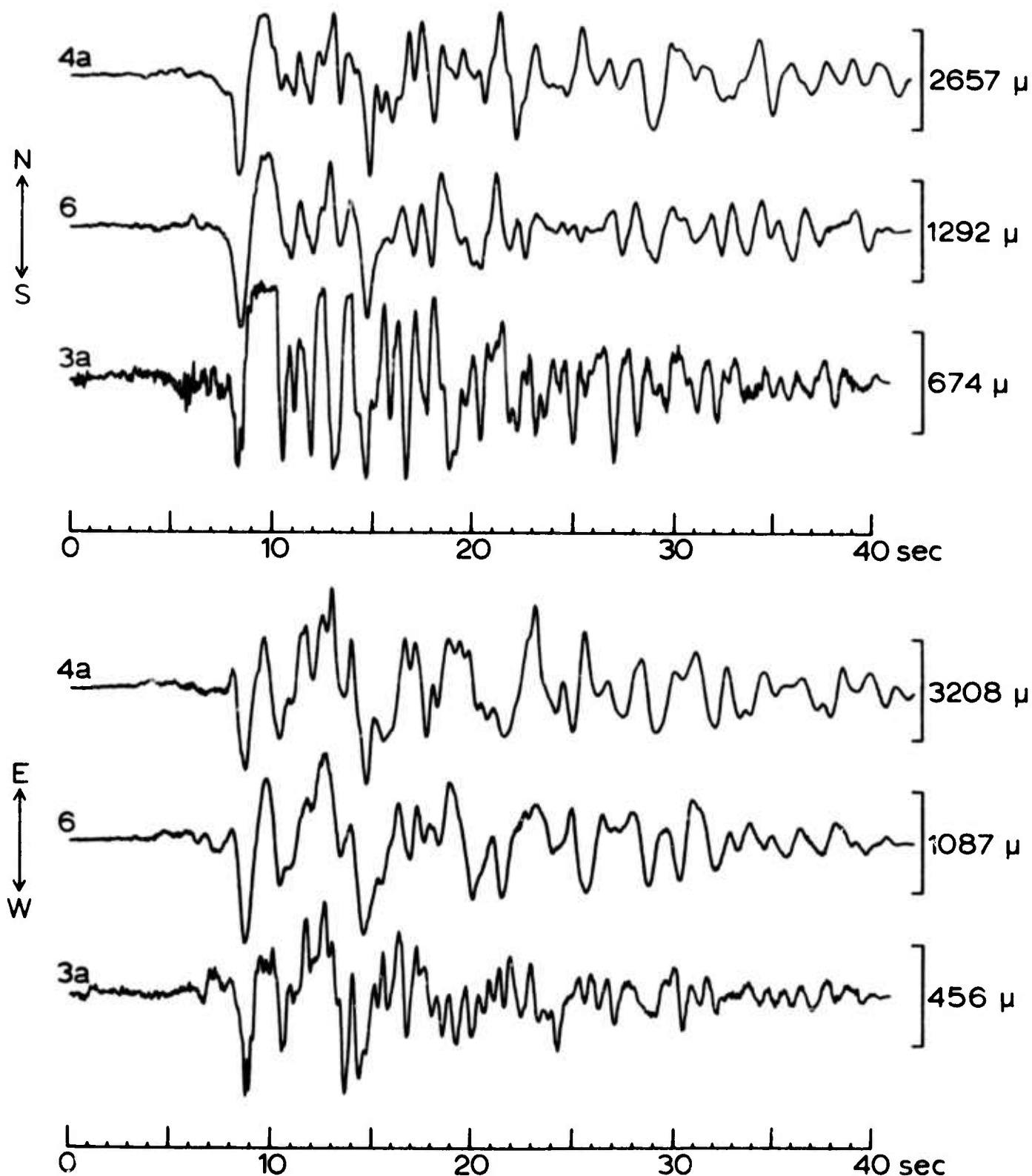


Figure 21. The displacement seismograms recorded at SAGO-East from events 4a, 6, and 3a (Table 1) at epicentral distances of 31, 22, and 15 km, respectively. The seismograms have been aligned for coincidence of the S pulse at about 8 sec.

The coda and the mechanism by which it is generated has an effect upon the estimate of the seismic moment. A measure of this effect can be obtained by considering the moment estimates in Tables 2 and 3. Except for event 1 and to a lesser extent 2 where the effects of the radiation pattern are important, the frequency-domain estimates of moment in Tables 2 and 3 are approximately equal and the differences reflect the uncertainties in the estimates. However, there is a systematic difference between the frequency-domain and time-domain estimates in Table 3 which is due to the fact that the effect of the coda is included in the former but not the latter. Thus the difference is largest for the events with the largest codas, event 4a and event 7a at SAGO-East. The question of which of these estimates is the most appropriate for the seismic moment of the earthquake depends upon the interpretation given to the coda. If the S pulse on the seismograms has played a major role in generating its own coda through conversions along the propagation path, then the frequency-domain estimate is most appropriate. If on the other hand the coda is mainly the result of scattering and multi-pathing, then the time-domain estimate is most appropriate. The best interpretation most likely lies somewhere between these two extremes.

An interesting aspect of the spectra presented in this study (Figures 4, 6, 10, 15, 17, and 20) is the diversity in the shape of the spectra, particularly toward the low frequencies. Examples of sloping, flat, and peaked spectra are all present, often for the same earthquake. Equally significant is the fact that the spectra of the synthetic seismograms also show this varied behavior even though a spectrum which is flat at frequencies less than the corner frequency is to be expected on the basis of the source function used in the calculations. This demonstrates that

the shape of the spectrum is strongly affected by the interference of various arrivals on the seismogram, and that in general the shape of the spectrum computed from a seismogram is not a good estimate of the shape of the source spectrum, particularly in the details of the low-frequency portion.

It now remains to consider briefly some of the implications and interpretations of the foregoing results with respect to the physical processes involved at the earthquake source. In most recent studies the corner frequency is considered to be inversely proportional to the dimension of the source. A number of different relations are available with slightly different proportionality constants (see Hanks and Wyss (1972) and Wyss and Hanks (1972) for further references and discussion), but the relation of Brune (1970, 1971) is the most widely used and gives the radius of the source as

$$r = \frac{2.34 \beta}{2 \pi f_0} \quad (6)$$

The source diameters listed in Table 4 were calculated with this formula and the average corner frequency of each earthquake in Table 2. Also listed in Table 4 is the stress drop calculated according to the relation of Brune (1970)

$$\Delta \sigma = \frac{7M_0}{16r^3} \quad (7)$$

and the average fault dislocation calculated from the relation

$$\bar{u} = \frac{M_0}{\pi \rho \beta^2 r^2} \quad (8)$$

Comparing values of $2r$ from Table 4 with various estimates of fault length for earthquakes of similar magnitudes, one finds a general agreement with some studies (McEvilly, 1966; Press, 1967) but disagreement with others

Table 4. Estimated source parameters

Event	M_L	2r km	$\Delta\sigma$ bars	\bar{u} cm
1	4.6	1.6	100	26
2	4.7	1.2	90	18
3a	4.0	1.4	36	8
3b	2.6	1.1	1	.2
3c	3.7	2.0	7	2
3d	2.4	1.2	0.5	.1
4a	5.1	2.0	280	90
4b	3.6	0.9	25	4
5	4.7	1.7	64	17
6	4.7	2.2	44	15
7a	4.9	1.7	102	27
7b	4.1	1.7	11	3
7c	3.0	1.2	2	.5

(Wyss and Brune, 1968; Thatcher, 1972). More significant is the trend in the data which indicates a weak dependence of source dimension upon magnitude; this is discordant with published relations such as those of Press (1967), Bonilla (1970), and Wyss and Brune (1968). Note, however, that the trend in these data is quite similar to the results of Thatcher (1972) for earthquakes in northern Baja California. The stress drops and average dislocations tabulated in Table 4 are both strongly dependent upon magnitude. These results are direct consequences of the fact that for these central California earthquakes the corner frequencies are only weakly dependent upon magnitude (equation 4) while the seismic moments are strongly dependent upon magnitude (equation 2).

A possibility which must be considered is that the corner frequencies observed in this study do not represent the interference effect due to the dimension of the earthquake source. One of the purposes of SAGO is to acquire information about the dimension and propagation of earthquake sources by making observations at different azimuths in the near field, but no evidence that explicitly requires these properties has been uncovered so far in the present study. In fact, some of the data may be inconsistent with the hypothesis relating corner frequency to source dimension. Consider the three similar earthquakes: events 3a, 4a, and 6 (Table 1). According to McNally (1973) the aftershocks of these earthquakes are spread out along the San Andreas fault for distances of about 2.5, 7, and 4 km, respectively. On the basis of these results and the commonly accepted suggestion of Benioff (1955) that the aftershock zone is a measure of the portion of the fault involved in the main shock, one would expect the corner frequencies to vary by a factor of almost 3 among these earthquakes. But inspection of the values in Table 2 and the seismograms in Figure 21 shows that this is not the case.

An alternative hypothesis is that the corner frequency is due to the rise time of the source function such as was assumed for the sake of convenience in the synthetic calculations. No data have been uncovered in the present study which are inconsistent with this hypothesis.

Comparing the rise times used to obtain the fits between observed and synthetic spectra (Table 3 and Figures 10, 15, 17 and 20) with the observed corner frequencies (Table 2) shows that the inverse of the corner frequency is a fairly good estimate of the rise time.

A surprising result of this study is that, except for the seismic moment, the source parameters of these central California earthquakes show little variation over the magnitude range from 3 to 5. At the same time it is clear that these results can not be simply extrapolated to larger magnitudes. For instance, the 1966 Parkfield earthquake with a M_L of 5.5 exhibited clear evidence in both spectra and surface faulting for a source length of 20 to 40 km, and this would imply a corner frequency much lower than the relation given in Figure 8 and equation 4. While the final answer to this interesting dilemma must await further study of earthquakes in the magnitude range greater than 5, several intriguing possibilities suggest themselves. First, as the magnitude increases beyond about 5 the corner frequency will become less than the natural frequency of the Wood-Anderson seismometer (1.2 Hz), and thus the nature of the M_L magnitude scale and its relation to source parameters could be quite different at these larger magnitudes. Second, the relation between source dimension and magnitude may be a very nonlinear one with a threshold around magnitude 5 above which much longer ruptures can occur. This threshold may represent that value of M_L for which the entire brittle zone of the crust (say from 3 to 10 km) becomes involved in the rupture. Finally, there is the possibility that the corner frequencies of this study are actually due to rise time, but that a separate relation between corner frequency and source dimension having a much stronger dependence upon magnitude begins to dominate (i.e., lower f_0) at magnitudes above 5.

CONCLUSIONS

The large amount of data and attendant discussion presented in this paper can be summarized in the following conclusions.

- 1) Fault plane solutions separate the earthquakes of this study into two different groups in terms of their tectonic characteristics. Earthquakes on or southwest of the San Andreas fault are consistent with north-south compression and the general picture of right-lateral movement on the northwest trending San Andreas fault. Earthquakes northeast of the San Andreas fault have compressional axes oriented in a northeast-southwest direction and are consistent with right-lateral movement on fault planes parallel to the more northerly trending Calaveras fault.
- 2) Broadband recording systems such as those at SAGO provide a very useful type of data for earthquakes recorded in the near field. For earthquakes involving up to several mm of ground motion, useful information has been obtained in the frequency band from 0.03 to 10 Hz.
- 3) The difficulties of isolating various individual seismic arrivals on near-field seismograms for the purpose of computing spectra can be satisfactorily circumvented by the use of whole-record spectra. Such whole-record spectra can be used to obtain reliable and consistent estimates of source parameters, although estimates of the seismic moment may be slightly inflated because of the effect of the coda.
- 4) Synthetic seismograms and spectra calculated with extremely simple models of the earthquake source and crustal structure have proved useful in matching observed ground motion as well as indicating those features of the data not predicted by the simple theory and thus of particular interest. These synthetic results also provide a systematic

and consistent method of estimating seismic source parameters in either the time domain or frequency domain.

5) Care must be taken in the interpretation of the low frequencies of near-field spectra. The synthetic results show that even when the source spectrum is flat at low frequencies the spectra computed from seismograms may not be flat in the bandwidth recorded. In addition, there are several ways in which spurious low-frequency behavior can be introduced into the spectra through the effects of tilts, flexing or movement of the seismometers on their bases, or nonlinear modes of vibration in the seismometer. All of these effects should be considered in near-field instrumentation.

6) The results of this study show that the seismic source moment can be estimated from near-field data with an uncertainty factor of about 2. This uncertainty does not include the effect of geology at the recording site which can contribute another factor of at least 3. When plotted against magnitude the $\log(\text{moment})$ of the earthquakes in this study exhibit a linear relation in the magnitude range of 2.5 to 5 with a slope slightly greater than 1.

7) All of the spectra obtained in this study have corner frequencies in the range of 1 to 3 Hz. Reliable estimates of the corner frequency and high-frequency slope are often difficult to obtain and depend upon the method of estimation and assumptions made about attenuation. The corner frequencies estimated in this study contain an uncertainty of about 30%. The high-frequency slope of the spectra on a log-log plot is typically about -2. Although the scatter in the data is considerable, there appears to be a weak dependence of the corner frequency upon magnitude. In principle, it is also possible to obtain an estimate

equivalent to the corner frequency from the duration of the S pulse on the seismograms, but in practice this procedure can yield misleading results because of the apparent multiple nature of the S pulse on some seismograms.

8) If the corner frequencies of the spectra are interpreted in terms of the dimension of the earthquake source, then the earthquakes of this study have source dimensions of about 1 to 2 km with a weak dependence upon magnitude. The theory of Brune (1970) applied to these data leads to stress drops between 1 and 280 bars with a strong dependence upon magnitude. An alternative explanation is that the corner frequencies observed in this study are related to the rise time of the source function.

ACKNOWLEDGMENTS

The unique data used in this study are available because of the commitment of the Seismographic Station of the University of California to the concept of a long-term special purpose observatory such as SAGO. Numerous individuals have contributed to this effort over the years, beginning with Professor Bruce Bolt who initiated the idea in 1964 and the Howard Harris family who donated the land and have provided invaluable assistance in constructing and operating the observatory. The National Science Foundation and the U. S. Geological Survey provided financial support for the initial installation. The present study was supported by the Advanced Research Projects Agency of the Department of Defense and was monitored by the Air Force Office of Scientific Research under Contract No. AFOSR-72-2392.

REFERENCES

- Benioff, H. (1955). Mechanism and strain characteristics of the White Wolf fault as indicated by the aftershock sequence, in Earthquakes in Kern County California During 1952, Bulletin 171, California Division of Mines, San Francisco, p. 199-202.
- Bolt, B. A., C. Lomnitz, and T. V. McEvilly (1968). Seismological evidence on the tectonics of central and northern California and the Mendocino escarpment, Bull. Seism. Soc. Am., 58, 1725-1767.
- Bolt, B. A. and R. D. Miller (1971). Seismicity of northern and central California, Bull. Seism. Soc. Am., 61, 1831-1847.
- Bonilla, M. G. (1970). Surface faulting and related effects, in Earthquake Engineering, R. L. Wiegel (ed), Prentice-Hall, Englewood Cliffs, N.J., p. 47-74.
- Bracewell, R. (1965). The Fourier Transform and Its Applications, McGraw-Hill, New York, 381 p.
- Brune, J. N. (1970). Tectonic stress and the spectra of seismic shear waves from earthquakes, J. Geophys. Res., 75, 4997-5009.
- Brune, J. N. (1971). Correction (to Brune, 1970), J. Geophys. Res., 76, 5002.
- Chuaqui, L. and T. V. McEvilly (1968). Crustal structure within the Berkeley array, paper presented at the annual meeting of the Seismological Society of America, Tucson, Arizona, April 11-13.

- Gutenberg, B. (1956a). Effects of ground on shaking in earthquakes, Trans. Amer. Geophys. Union, 37, 757-760.
- Gutenberg, B. (1956b). Comparison of seismograms recorded on Mount Wilson and at the Seismological Laboratory, Pasadena, Annales de Geophysique, 12, 202-207.
- Gutenberg, B. (1957). Effects of ground on earthquake motion, Bull. Seism. Soc. Am., 47, 221-250.
- Hanks, T. C. and M. Wyss (1972). The use of body-wave spectra in the determination of seismic-source parameters, Bull. Seism. Soc. Am., 62, 561-589.
- Johnson, L. R. (1974). Green's functions for Lamb's problem, Geophys. J. R. Astr. Soc., in press.
- Kurita, T. (1973). Attenuation of shear waves along the San Andreas fault in central California, paper presented at the Conference on Tectonic Problems of the San Andreas Fault System, Stanford University, June 20-23.
- Litehiser, J. J. (1974). Near field seismograms from a propagating dislocation, PhD Thesis, University of California, Berkeley.
- McEvelly, T. V. (1966). The earthquake sequence of November 1964 near Corralitos, California, Bull. Seism. Soc. Am., 56, 755-773.
- McNally, K. (1973). Some behavioral details of seismically active segment of San Andreas fault in Stone Canyon-Bear Valley area, in Tech. Rept. No. 2, Grant AFOSR-72-2392, University of California, Berkeley.

- O'Neill, M. E. and J. H. Healy (1973). Determination of source parameters of small earthquakes from P-wave rise time, Bull. Seism. Soc. Am., 63, 599-614.
- Press, F. (1967). Dimensions of the source region for small shallow earthquakes, in Proceedings of the VESIAC Conference on the Current Status and Future Progress for Understanding the Source Mechanism of Shallow Seismic Events in the 3 to 5 Magnitude Range, University of Michigan, Ann Arbor, p. 155-164.
- Thatcher, W. (1972). Regional variations of seismic source parameters in Northern Baja California area, J. Geophys. Res., 77, 1549-1565.
- Wyss, M. and J. N. Brune (1968). Seismic moment, stress, and source dimensions for earthquakes in the California-Nevada region, J. Geophys. Res., 73, 4681-4694.
- Wyss, M. and T. C. Hanks (1972). The source parameters of the San Fernando earthquake inferred from teleseismic body waves, Bull. Seism. Soc. Am., 62, 591-602.

FIGURE CAPTIONS

Figure 1. A map of part of central California showing the primary mapped fault traces, the locations of the seismographic stations at SAGO-Central and SAGO-East, and the epicenters of the 13 earthquakes studied. The identification numbers key the earthquakes to Table 1. The open triangles associated with the larger earthquakes denote the directions of principal compression as determined from fault plane solutions (Figure 2).

Figure 2. Upper hemisphere projections of the polarity of P waves from 7 of the larger earthquakes in Table 1 and the fault plane solutions determined on the basis of these data. Circles denote compressions and triangles denote dilatations. Arrows indicate the horizontal projections of the principal compressive stress. The identification numbers key the earthquakes to Table 1 and Figure 1.

Figure 3. The displacement response functions of three types of seismographs at SAGO which were used in this study. The ordinate is in terms of output from a ± 2048 count A/D system.

Figure 4. The displacement seismograms and spectra recorded at SAGO-East (top) and SAGO-Central (bottom) from event 7b (Table 1). The plots of spectra show the amplitude density spectra for both signal (solid line) and an estimate of the noise (dashed line).

Figure 5. Templates used to obtain spectral estimates of the low-frequency level Ω_0 and the corner frequency f_0 for the cases where the high-frequency slope is -2 (left) and -3 (right) and for four values of t^* .

Figure 6. Example illustrating two different estimates of the low-frequency level Ω_0 and the corner frequency f_0 of the spectrum from the NS component at SAGO-East from event 6 (Table 1).

Figure 7. Relation between seismic moment and magnitude. The solid line was fit to the data points by linear regression and the dashed line is from Wyss and Brune (1968). The SAGO-East values have been divided by a factor of 3 to remove an amplification effect.

Figure 8. Relation between corner frequency and magnitude (top) and between corner frequency and log moment (bottom). In both graphs the line was fit to the data points by linear regression.

Figure 9. The displacement seismograms (solid lines) from event 1 (Table 1) recorded at SAGO-Central (top 2 traces) and at SAGO-East (bottom 2 traces). The dotted lines are synthetic seismograms calculated for this earthquake.

Figure 10. Amplitude density spectra calculated for event 1 (Table 1) from seismograms (Figure 9) recorded at SAGO-Central (top 2 spectra) and at SAGO-East (bottom 2 spectra). The solid lines are calculated from the observed seismograms, the dashed lines are estimates of the noise, and the dotted lines are calculated from the synthetic seismograms.

Figure 11. The predicted outputs of the displacement seismographs at SAGO-Central (top 2 traces) and at SAGO-East (bottom 2 traces) due to the elastic tilts calculated for event 1 (Table 1). The amplitudes on the right are equivalent ground displacements. The earthquake model used in this calculation is identical to that used for the synthetic results in Figures 9 and 10.

Figure 12. The displacement seismograms from event 1 (Table 1) recorded at SAGO-Central (top 2 traces) and at SAGO-East (bottom 2 traces). The dotted lines are the synthetic seismograms of Figure 9 with an additional negative impulse in tilt at the arrival time of the S wave.

Figure 13. Amplitude density spectra calculated for event 1 (Table 1). The solid and dashed lines are identical to those of Figure 10 but the dotted lines are calculated from the synthetic seismograms of Figure 12 which include the effects of an impulse in tilt.

Figure 14. The displacement seismograms (solid lines) from event 2 (Table 1) recorded at SAGO-Central (top 2 traces) and at SAGO-East (bottom trace). The dotted lines are synthetic seismograms calculated for this earthquake.

Figure 15. Amplitude density spectra calculated for event 2 (Table 1) from seismograms (Figure 14) recorded at SAGO-Central (top 2 spectra) and at SAGO-East (bottom spectrum). The solid lines are calculated from the observed seismograms, the dashed lines are estimates of the noise, and the dotted lines are calculated from the synthetic seismograms.

Figure 16. The displacement seismograms (solid lines) from event 7a (Table 1) recorded at SAGO-Central (top 2 traces) and at SAGO-East (bottom 2 traces). The dotted lines are synthetic seismograms calculated for this earthquake.

Figure 17. Amplitude density spectra calculated for event 7a (Table 1) from seismograms (Figure 16) recorded at SAGO-Central (top 2 spectra) and at SAGO-East (bottom 2 spectra). The solid lines are calculated from the observed seismograms, the dashed lines are estimates of the noise, and the dotted lines are calculated from the synthetic seismograms.

Figure 18. The displacement seismograms recorded at SAGO-Central from events 7a, 7b, and 7c (Table 1) with magnitudes 4.9, 4.1, and 3.0, respectively.

Figure 19. The displacement seismograms (solid lines) from event 4a (Table 1) recorded at SAGO-Central (top 2 traces) and at SAGO-East (bottom 2 traces). The dotted lines are synthetic seismograms calculated for this earthquake.

Figure 20. Amplitude density spectra calculated for event 4a (Table 1) from seismograms (Figure 19) recorded at SAGO-Central (top 2 spectra) and at SAGO-East (bottom 2 spectra). The solid lines are calculated from the observed seismograms, the dashed lines are estimates of the noise, and the dotted lines are calculated from the synthetic seismograms.

Figure 21. The displacement seismograms recorded at SAGO-East from events 4a, 6, and 3a (Table 1) at epicentral distances of 31, 22, and 15 km, respectively. The seismograms have been aligned for coincidence of the S pulse at about 8 sec.